crystals

MDPI

Review

Advancements and Perspectives in Additive Manufacturing of Tungsten Alloys and Composites: Challenges and Solutions

Mehrdad Zarinejad [1,2,*], Yunxiang Tong [3,*], Mojtaba Salehi [4,*], Chengfa Mu [1], Nian Wang [2], Yonglong Xu [2], Sajjad Rimaz [5], Lintao Tian [1], Kai Xiang Kuah [6] and Xiaotong Chen [1]

1 Research and Development Institute, Wenzhou Hongfeng Electrical Alloy Co., Ltd., No. 5600, Oujin Avenue, Oujiangkou Industry Cluster, Wenzhou 325700, China; muchengfa@wzhf.com (C.M.); tianlintao@wzhf.com (L.T.); chenxiaotong@wzhf.com (X.C.)
2 Wenzhou Hongfeng Alloy Co., Ltd., No. 1633, Binhai First Avenue, Wenzhou Economic and Technology Development Zone, Wenzhou 325603, China; wangnian@wzhf.com (N.W.); xuyonglong@wzhf.com (Y.X.)
3 Institute of Materials Processing and Intelligent Manufacturing, College of Materials Science and Chemical Engineering, Harbin Engineering University, Harbin 150001, China
4 Additive Manufacturing Division, Singapore Institute of Manufacturing Technology (SIMTech), Agency for Science, Technology and Research (A*STAR), 5 Cleantech Loop, Singapore 636732, Singapore
5 Department of Chemical and Bimolecular Engineering, National University of Singapore, 4 Engineering Drive 4, Singapore 117585, Singapore
6 Department of Materials Science and Engineering, National University of Singapore, 9 Engineering Drive 1, Singapore 117575, Singapore; kxkuah@u.nus.edu
* Correspondence: mehrdad@wzhf.com (M.Z.); tongyx@hrbeu.edu.cn (Y.T.); mojtaba_salehi@simtech.a-star.edu.sg (M.S.)

Abstract: This review explores additive manufacturing (AM) for refractory tungsten (W) and its alloys, highlighting the primary challenges and determining factors in the AM of pure W, W alloys and composites. The challenges mainly arise from W's high melting point, low laser absorptivity, high thermal conductivity, high melt viscosity, high oxygen affinity, high ductile-to-brittle transition temperature, and inherent embrittlement, which lead to defects and anomalies in AM-produced parts. This review focuses on both processes and alloying strategies to address the issues related to densification, micro-cracking, and the resultant properties in W-based components. Cracking in additively manufactured W remains a persistent issue due to thermal stress, embrittlement, and oxide formation. Powder characteristics, process parameters, and thermal management strategies are crucial for W densification. Throughout the review, existing knowledge and insights are organized into comprehensive tables, serving as valuable resources for researchers delving deeper into this topic. Future research in W-AM should focus on understanding the interaction between AM process parameters and microstructural and material design. Advances in atomic-level understanding, thermodynamic modeling, and data analytics have the potential to significantly enhance the precision, sustainability, and applicability of W-AM.

Keywords: refractory alloys; tungsten alloys and composites; additive manufacturing; laser and electron beam melting; challenges and mitigation strategies

Citation: Zarinejad, M.; Tong, Y.; Salehi, M.; Mu, C.; Wang, N.; Xu, Y.; Rimaz, S.; Tian, L.; Kuah, K.X.; Chen, X. Advancements and Perspectives in Additive Manufacturing of Tungsten Alloys and Composites: Challenges and Solutions. *Crystals* **2024**, *14*, 665. https://doi.org/10.3390/cryst14070665

Academic Editor: Umberto Prisco

Received: 4 June 2024
Revised: 15 July 2024
Accepted: 17 July 2024
Published: 20 July 2024

1. Introduction

Refractory alloys, including tungsten (W) and its alloys, are integral to aerospace and energy-generation industries [1]. W is well known for its high melting point (approximately 3422 °C), good mechanical properties, and low thermal expansion coefficient of less than 4 µm/m·K [2]. Additionally, its impressive thermal conductivity, surpassing 150 W/m·K [2], exceptional resistance to heat and wear [3], notable chemical stability, and remarkable hardness [3] make W suitable for high-temperature and radiation-resilient applications. Examples of its applications include collimators, heat sinks [4], integrated circuits [5,6], switch contacts [7], rocket nozzles [5,8], turbine blades [5], and nuclear reactor parts [5,9].

Harnessing the full potential of refractory alloys, particularly those of W-based materials, has been challenging owing to their high melting points and complex metallurgical behavior [10].

Conventional production methods for W-based alloys primarily rely on powder metallurgy techniques, which require high-temperature sintering. Achieving full densification is particularly challenging. Additionally, the hardness and brittleness of W alloys complicate formative and subtractive manufacturing processes, such as forming and machining methods. Furthermore, W oxidizes at relatively low temperatures (beginning around 400–500 °C), which increases the complexity and cost of manufacturing. Historically, the manufacturability of W-based alloys has been hindered by high costs, scalability issues, and challenges in producing intricate structures [11]. Additive manufacturing (AM) of refractory alloys offers unparalleled design freedom. Unlike traditional subtractive techniques that can waste up to 70% of material [12–14], AM's layer-by-layer approach ensures material efficiency, especially with costly refractory alloys [15,16].

AM could address some of the traditional challenges associated with the production of W-based alloys and provide significant advantages in terms of design flexibility, material efficiency, and the capability to create complex geometries. For instance, AM facilitates the production of intricate and custom molds for high-temperature tooling. As another example, AM allows for the creation of sophisticated channels and intricate geometries, enhancing the cooling efficiency of plasma-facing components in nuclear fusion reactors. Although W-AM can mitigate many of the issues associated with traditional techniques, the inherent properties of W alloys present significant challenges for AM processes. The high melting points and elevated ductile-to-brittle transition temperatures (DBTTs) pose concerns for all refractory alloys but are amplified for W because of its high viscosity (8×10^{-3} Pa·s) [17], surface tension (2.361 N/m) [17], and rapid solidification rate [18]. In the solid state, W's body-centered cubic structure adds complexity to thermal processes, particularly given its DBTT [19,20] and the notable influence of impurities on its DBTT. Issues such as interstitial contamination, balling [21], cracking [22], and the limited understanding of process-structure-property relationships [18,21,23] represent substantial hurdles to overcome.

Over the past decade, extensive research has been undertaken on the AM of unalloyed and alloyed W, as well as W-matrix composites [24,25]. Most studies on unalloyed W have utilized Powder Bed Fusion (PBF) processes, namely, Selective Laser Melting (SLM) [8,17–19,21,24,26–61], and Electron Beam Melting (EBM) [33,34,47,59–69] of W. Other notable methods employed include Direct Energy Deposition (DED) processes, namely laser-based DED [2,34,47,59–61,70–77] and electric arc-based DED [78,79], and binder jetting (BJ) which shows promise for W-based materials [80–84]. Other novel methods such as ultrashort-time liquid phase sintering (LPS) [85], and bound metal deposition (BMD) have also been introduced [86].

In most AM processes, W materials initially melt, and then solidify, leading to nucleation and subsequent grain growth. This thermal history contrasts with traditional processing techniques like sintering, which primarily deal with powder densification followed by sintering and grain growth. Post-solidification grain growth in AM shares similarities with sintering and is guided by kinetic laws [60,87]. However, in AM of nano-W, surface diffusion prevails [60,88], unlike traditional sintering's grain boundary diffusion. Recognizing these differences and understanding the influence of process parameters and alloy chemistry on molten pool behavior, solidification, and further solid-state microstructural evolution and strengthening effects are essential for advancing the field of W-AM [24,60,74,89–91].

Building on the foundation of previous review articles on W-AM [58,60,61], our review delves deeper into understanding process parameters' design and recent advancements in materials design strategies aimed at mitigating W-AM challenges. We begin by providing an overview of the current status of AM techniques for W alloys, focusing on the PBF, DED, and BJ processes. We will then look at the challenges that are often associated with their AM

processes, such as densification, microcracking, and limited material properties, followed by mitigation strategies that researchers have developed from both design and material perspectives to address these issues. Finally, our review concludes with an exploration of promising future directions for W-AM, aimed at paving the way for broader adoption and commercialization.

2. Techniques for Additive Manufacturing of W-Based Materials

W and W-based metal systems demand substantial energy input during AM. With technological advancements, AM systems have been equipped with high-energy sources like lasers and electrons to provide the energy required. Table 1 provides a brief comparison of process parameters and relative densities achieved via different AM techniques for W-based materials (pure, alloys, and composites). Figure 1 depicts the schematic setups of these methods [92–96]. The choice of an AM method for W materials depends on several factors including the material type, post-processing needs, geometric accuracy, cost, surface finish, and property requirements [33,61].

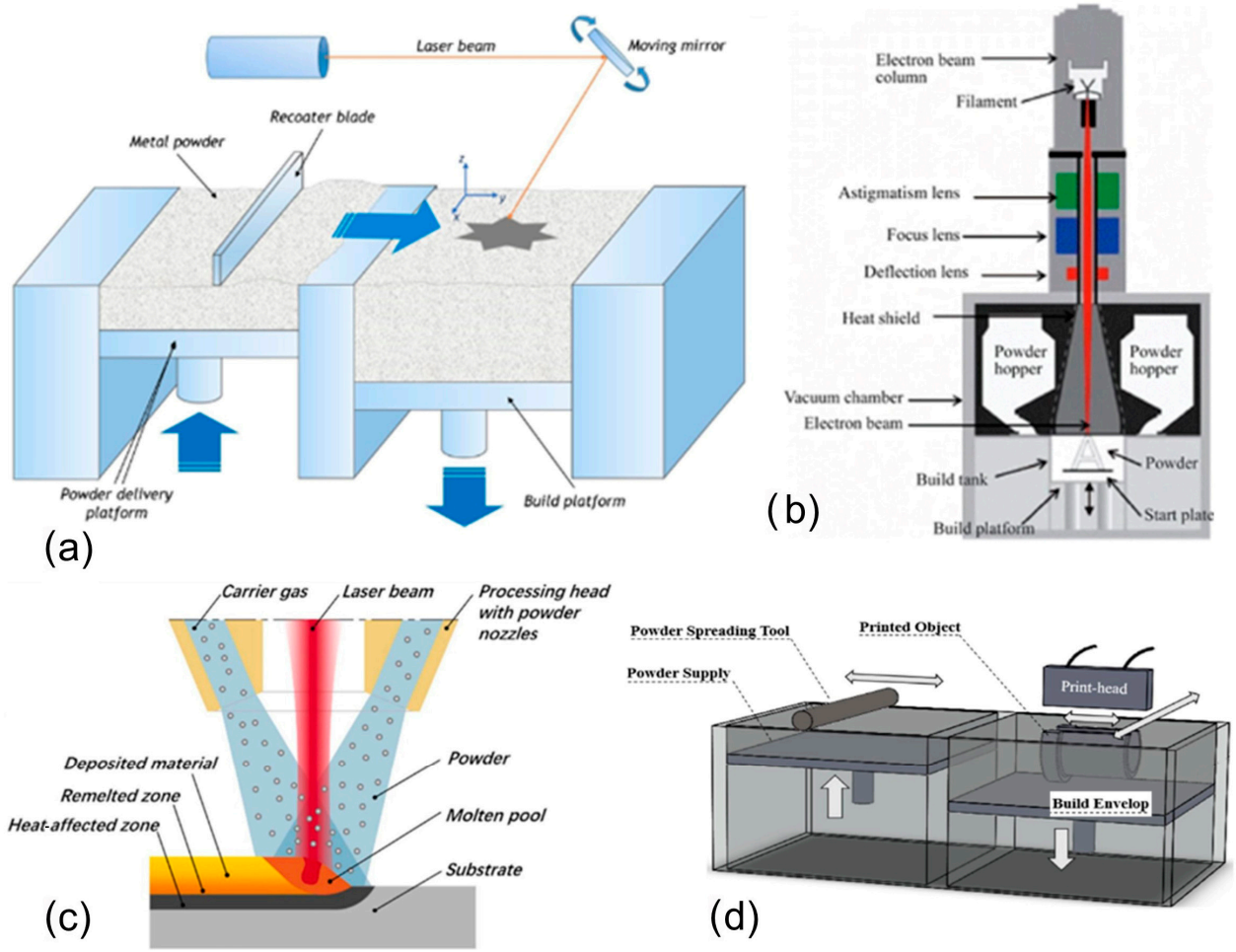

Figure 1. Schematic setups of AM techniques used in W materials fabrication: (**a**) SLM [92], (**b**) EBM [94], (**c**) laser-based DED [93], and (**d**) BJ [96].

SLM (Figure 1a) has been extensively studied for fabricating W and its alloys [97]. Crack forming, especially at grain boundaries, is a major issue in SLM-produced W parts. This happens because of factors such as rapid cooling creating thermal stresses exceeding DBTT, and oxygen trapped at the boundaries during the coalescence of the particles [19,29,63]. Nevertheless, SLM-fabricated W materials can achieve relative densities of 95% to 99.2% [30,47,54,98]. Advancements like femtosecond fiber lasers can potentially improve this technique [18].

Using the double melt strategy also improves W densification [46]. SLM has the potential for integration with other techniques (such as infiltration) to achieve higher density in W parts [19,60].

EBM (Figure 1b) is another prominent AM technique for W [94]. This method employs an electron beam as its primary heat source, which is manipulated through an electromagnetic lens, as detailed in Galati [62]. EBM requires a high vacuum level post He/N_2 purge due to electron travel [32,63]. In comparison to SLM, EBM offers a higher power level of powder [61,99], with typical values between 1000 and 3000 W [32,60,63]. This increased power is responsible for a relative density close to 99.5% in W materials [32]. With appropriate preheating, EBM can address cracking issues in AM for W materials [32,61,62], with many promising results from EBM-fabricated W being reported [32,60,61]. EBM has also been adapted for W surface treatment to enhance quality, due to its controlled beam size and thermal influence [69]. Despite the advantages of EBM, challenges in its use that include complexities associated with electron focusing and the need for maintaining a high vacuum remain [32].

Laser-based DED (Figure 1c) has the distinction of directly adding energy during processing [71–77,93]. In laser-based DED, the relationship between molten pool size and powder flow is crucial [4]. Although increased laser energy can widen the molten pool, when the molten pool exceeds the flow of the powder, it can result in a reduction in the percentage of W entering [2]. The high-energy laser beam rapidly heats and cools powders, which reduces the microstructural coarsening duration [71,76]. Laser-based DED, with its larger melt pools (about several mm) and reduced cooling rates [61,71,76,99], promotes W particle rearrangement and reduces porosity [72–75], while SLM-processed W materials show fusion deficiencies and non-uniform W particle distribution (despite powder preheating) that lead to brittleness. There remains a growing interest in laser-based DED for W alloys because it can produce materials with higher relative density compared to SLM. This improved performance is largely credited to the technique's larger laser spot size [6,31]. Challenges arise in laser-based DED such as managing surface roughness [70] and the formation of intermetallic compounds due to high energy inputs [31].

In BJ (Figure 1d), a flowable powder is laid onto a build platen, followed by the selective deposition of binder material in the shape of the intended part [96]. After each layer, the platen descends, a new powder layer is spread, and the procedure is repeated. These layers are adhered together to create the targeted component. Once the printing is finished, the build box undergoes a curing process in an oven to solidify the binder material [80–84]. The green body is subsequently separated from the surplus powder for further processing. Then, the part undergoes sintering, similar to a standard compacted W component. Tungsten Heavy Alloys (WHAs) with a relative density of 99.7% have been obtained via this method [80]. While the BJ method offers the significant advantage of stacking parts for mass production, achieving fully dense W parts is extremely challenging due to the necessity of high-temperature sintering.

In subsequent sections, we will discuss the AM of W-based materials, which includes pure W, W alloys, and W composites. In this review, we consider all combinations of W with other elements as alloys and refer to combinations of W with ceramic materials as composites. We begin by examining the factors and processing strategies involved in the AM of unalloyed W. We next highlight methods to address the challenges related to processing and properties. Following this, we discuss additively manufactured W alloys and composites, presenting alloying strategies and the role of dispersed ceramic phases (in the W composites) on AM processing, and the resulting properties of W alloys and composites.

Table 1. A brief comparison of AM processes for W-based materials.

AM Process	Energy (W)	Beam Size (μm)	Scan Speed (mm/s)	Temperature Gradient (°C/mm)	Cooling Rate (°C/s)	Relative Density (%)
SLM	10^2–10^3 (normally below 1000 [60,61,99])	30–200 [61,99]	10–1000 [99]	10^6–10^7 [61,99]	10^5–10^7 [61,99]	99.2 [98]
EBM	10^2–10^3 [61,99] (normally more than 1000 W, up to 3000 W [32,60,63], but can be as high as 6000)	100–1000 [61,99]	10–1000 [99]	-	10^3–10^4 [61,71,99]	~100 [100]
Laser-based DED	10^2–10^4 [71,99] (normally between 600 and 4000 [61])	100–1000 [61,71,76,99]	10–1000 [61,76,99]	10^4–10^6 [61,71,99]	10^2–10^5 [99], mostly on the order of 10^4 °C/s [19]	More than 99 for W [2]: even higher for W alloys [31]
BJ (Binder Jetting) [80–84]	Not applicable	Not applicable	Not applicable	Not applicable	Not applicable	99.7 for WHA [80]

3. Additively Manufactured Unalloyed W: Challenges, Determining Factors, and Mitigating Strategies

3.1. Problems and Resolutions in Brief

The remarkable properties of unalloyed W, including its exceptional melting point and high thermal conductivity, make it highly desirable in different applications. However, problems associated with the AM of W still need to be overcome. This section will briefly introduce key challenges and look at their potential solutions (Table 2). The mechanical properties of additive-manufactured unalloyed W, particularly its elongation, tensile strength, and fracture toughness, often fall short of expectations. Researchers have found ways to improve these properties through targeted alloying, the inclusion of ceramic reinforcements, and optimizing the parameters used during the AM process itself [49].

W is inherently brittle due to its high Peierls stress that stems from its BCC crystal structure and weak grain boundary cohesion. The ductility of W can be improved through appropriate alloying, which improves the stacking fault energy of the microstructure to enhance the slip mechanism [60]. The inherent brittleness of W is further exacerbated by its high DBTT, thermal stresses, and oxygen-induced grain boundary issues, all of which led to cracking during the AM process. While strategies like alloying, incorporating carbide/oxide reinforcements, and process adjustments have shown some promise in improving the ductility of additively manufactured W, further studies are needed to completely eradicate these cracking problems [21,38,49].

Another problem stems from the confluence of W's high melting point, low laser absorptivity (<70% in SLM), and high viscosity, making it difficult for powders of W and alloying elements to properly melt and fuse during the printing process. Furthermore, the AM process can be plagued by phenomena like balling, where molten material forms spheres instead of adhering properly. The selection of W powders with improved laser absorption and optimization of processing parameters can mitigate these issues [30,38,40,41,43,51,53,101]. Optimizing process control parameters, particularly laser power and scan variables, has been shown to be instrumental in achieving better densification of W parts [30,38,41,102].

W's propensity for oxygen poses another challenge, as it leads to the formation and incorporation of W oxide and subsequent hot cracking during AM. There are limited options for mitigating the oxidation of W during AM, including the use of high-quality starting materials, establishing better processing atmospheres, and using specific alloying combinations [49].

Table 2. An overview of the primary challenges, governing factors, and potential or attempted mitigation strategies in the AM of W.

Challenges	Possible Strategy/Developments to Tackle the Challenge	Reference
The inherent brittleness and low ductility of W stem from (1) the high Peierls stress of its BCC crystal structure and (2) weak grain boundary cohesion.	Requires appropriate alloying to increase stacking fault energy for easier slip, and microstructural optimization.	[60]
High melting point, significant laser absorptivity (<70% for SLM), pronounced viscosity, densification, porosities, balling, and deformation.	Use of smaller, spherically shaped W powders to enhance laser absorptivity; adjusting processing parameters to influence outcomes like defects, densification, and grain structures. Optimizing parameters like power and volumetric energy density have been found pivotal for improved W densification.	[30,38,40,41,43,53,71,102]
Oxygen affinity and W oxide segregation lead to hot cracking.	Better quality starting material (powder, wire) production, optimized processing atmosphere, alloying.	[49]
Cracks due to W embrittlement and high DBTT; thermal stress-induced, difficult-to-control crystallization; and oxygen-induced cracking along the grain boundaries.	Adjusting laser speeds and reducing grain sizes; techniques to adjust laser speeds and reduce grain sizes showed some positive results but did not completely resolve the issue. Scanning strategy optimization: speed, rotation, remelting.	[8,19,21,38,45,49]
Mechanical property issues (tensile strength and limited fracture toughness) especially in SLM-fabricated W.	Alloying, introduction of reinforcements, process adjustments.	[49]

3.2. High Melting Point, Related Challenges, and Controlling Strategies

W's intrinsic high melting point can result in pronounced thermal gradients during AM. Rapid heating and cooling cycles lead to thermal distortion, significant residual stresses, and crack initiation. This compromises the mechanical integrity of the printed components. Furthermore, W exhibits high thermal conductivity. In AM, this causes rapid heat dissipation, complicating the sustenance of the molten state, leading to partial melting and inconsistent fusion. These characteristics can influence the resultant component's microstructure and mechanical properties [29,41,42,53,67]. In the case of alloyed W, the evaporation of low melting point elements can also be a challenge. Working at elevated temperatures also demands more of AM machinery, leading to heightened maintenance needs and increased costs [61,103]. Concurrently, the susceptibility of W and its alloys to oxidation increases at high temperatures, often leading to surface oxide formations that undermine material performance [49].

3.2.1. Melting

Melting behavior is integral to W-AM, often serving as a key factor that defines its AM processing window. The direct melting of W presents significant challenges due to the practical constraints associated with high laser power sources and the large beam sizes required. The very high melting point of W necessitates powerful laser systems capable of delivering sufficient energy for melting. These systems often require power sources that are not commonly available in standard AM machines. Additionally, the large beam sizes needed to ensure adequate energy distribution across the W powder bed can lead to significant thermal gradients, causing residual stresses and potential cracking. The combination of high laser power and large beam sizes also limits the precision and resolution of the final parts. Such strict criteria lead to many partial melting situations, making it difficult to fabricate high-quality parts [52]. The particle size and morphology of W powder, layer thickness, heat source power, volumetric energy density controlled by scanning variables and strategies, melting behavior, and interfacial characteristics are all important in the melting of W during AM processing.

Particle Size and Morphology

Several powder characteristics are decisive for W-AM, especially for PFB processes [104,105]. The primary factors include powder particle morphology, particle size, and purity. Particle size and morphology significantly influence the flowability of the powder and the resulting powder bed density, which in turn influences the density and mechanical properties of the final component. Smaller particle sizes generally lead to better packing density and surface finish but may increase the risk of oxidation and require higher laser energy due to an increased surface area. The shape of the powder particles (spherical vs. irregular) directly impacts the flowability such that spherical particles tend to flow more easily and pack more densely than irregularly shaped particles, resulting in a consistent layer formation during the built cycle. The purity of the powder is critical in avoiding contamination that can lead to defects in the final product. Impurities can cause the formation of brittle phases, reduce ductility, and introduce cracks or other anomalies in AM-fabricated parts.

W's inherent properties necessitate the modification of its powders. These adjustments are needed to improve morphology, ensure uniform size, maximize laser absorption [26], and enhance surface conditions. Techniques such as the utilization of radio frequency plasma have been employed for these modifications [26,27]. The modifications are critical for powder flowability and to achieve a desired density [27]. Zhang et al. studied the influence of particle size on laser absorptivity [53], finding absorptivity to be higher when the powder bed was on a substrate because of incident laser ray entrapment. As an example, a 5 µm powder natively had 0.53 absorptivity but this increased to 0.603 on a stainless steel substrate. Finer particles increase absorptivity, which is the ability of a material to absorb energy from the laser or electron beam, due to their higher surface area-to-volume ratio. Fine powders can also enhance printability by improving detail resolution, packing density, and surface finish. Notably, printability is a comprehensive measure of how effectively a material can be used in a given AM process. It is influenced by a variety of factors, including powder material properties, machine capabilities, process parameters, and design considerations.

Given the cost and limited availability of fine powder sizes, Wang et al. [26] explored an alternative approach to enhance W powder absorptivity. They managed to transform irregularly shaped powder particles into near-perfect spheres (close to 100% sphericity) using radio frequency (RF) induction plasma. These spherical particles were significantly smaller (average size of 31.5 µm) compared to the raw powder (average size of 56.8 µm). This transformation resulted in a significant increase in absorptivity, exceedingly not only in the raw powder (as shown in Figure 2) but also exceeding the values predicted by Zhang et al. [53]. Very fine particles with an average size of 17.3 µm were used to successfully obtain continuous tracks without cracks [29]. However, it is important to note that studies have not established a direct correlation between particle size and achieving crack-free tracks of pure W.

Power, Volumetric Energy Density, Layer Thickness

Volumetric energy density (*VED*) is a crucial parameter in AM design, as it plays a decisive role in defining processing parameters. This can be mathematically represented in Equation (1), where the *VED* is expressed as follows [106,107]:

$$VED = P/(v \times s \times t) \quad (1)$$

where P is the laser power, v is the laser scanning speed, s is the hatch spacing, and t is the layer thickness. The energy input required for AM varies depending on the specific AM processes, machine parameters, material characteristics, and part geometries. Due to the interplay of these factors, a single, universal value for energy input in the AM of a material cannot be established. These variations are reflected in the reported literature, where a wide range of energy input values is observed for W-based materials (e.g., 400 J/mm^3,

8.595 J/mm^3, 1000 J/mm^3). These variations highlight the importance of considering the specific experimental conditions under which such values were determined. Table 3 offers an overview of the VED's effect on W-AM.

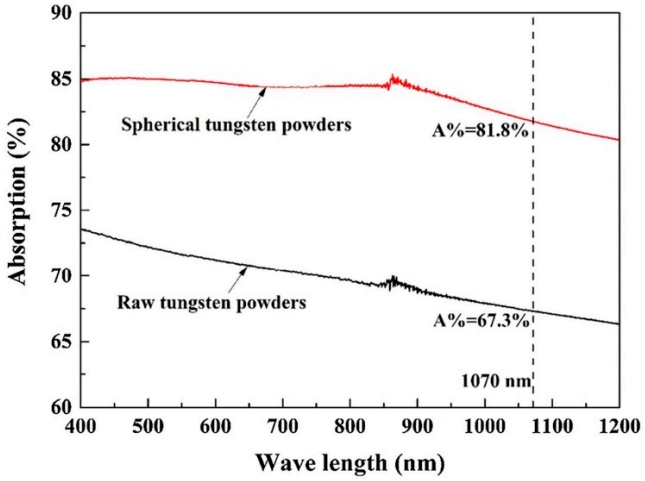

Figure 2. Comparison of absorption properties between non-spherical (raw) and spherical W powders [26]. Reproduced with permission from Elsevier.

Sidambe and Fox [108] as well as Sidambe et al. [36] investigated the impact of VED on the relative density of W parts. Both studies found relative density to increase with higher VED, although the latter reported even higher relative density values at the same VED (Figure 3a). Guo et al. [41] and Hu et al. [42] examined the impact of VED on relative density and hardness using spherical particles. They found that increasing VED led to increased relative density and decreased pore size to achieve a maximum relative density of approximately 98.3%. Microhardness also increased with higher VED, reaching values of 474 Hv [41] and 430 Hv [42]. Other studies on SLM, however, reveal the complexity of the influence of VED and laser power. Yamamoto et al. investigated how laser power, scanning speed, and hatch spacing affect the density of W cylinders [50]. The parts printed from pure polyhedral W powder at a preheating temperature of 35 °C showed that higher laser power and wider hatch spacing led to denser parts, matching the results of those from Rebesan et al. [37]. Plotting the VED against relative density showed the highest relative density reached was 98.58% at a VED of 411 J/mm^3 (P = 370 W, v = 500 mm/s, h = 90 µm, t = 20 µm; Figure 3b). This VED trend differed from those of Guo et al. [41] and Enneti et al. [51], who reported increasing relative density within the VED range. This difference highlights the uncertain role of VED in relative density estimation. Hatch spacing and scanning strategy affect part integrity, porosity type, and thermal history for each layer. Thus, interpreting these trends requires a full understanding of each study's parameters and specific porosity characteristics [50,58]. Wen et al. [30] studied the fabrication of W cubes with varying laser power, scanning speed, and hatch spacing. They found the use of low laser power to result in dense, high-relative-density cubes due to the laser's impact on melt pool temperature. Increasing the line (laser) energy density (LED) led to warped morphologies, which were eliminated with a further increase in LED due to stronger interlayer bonding. Cracks were observed but reduced with higher scanning speed, reaching a maximum relative density of 98.71% at 200 mm/s scanning speed.

For W materials, a higher VED and subsequent higher processing temperature may reduce the resultant residual stresses due to enhanced annealing effects [60,109]. This reduction in residual stresses might be why using EBM generally leads to a reduced cracking probability in W materials when compared to using SLM [63]. Extremely high VEDs (e.g., >300 J/mm^3) are not necessarily beneficial (Figure 3c) [19,50,110]. Density in AM-produced W parts is influenced by several factors. One issue is unstable laser melting. The intense laser beam can create deep holes, called keyholes, that do not fully solidify,

leaving air pockets (porosity) throughout a part [19]. Another problem arises from using too much laser power. Excessive melting disrupts the molten metal pool, trapping air bubbles and reducing density [32]. Powder characteristics can also be problematic. If particles do not flow smoothly into the melt pool but instead stick to the edges, they create voids and hinder densification [32]. Finally, W's high melting point presents another hurdle. Some elements that evaporate easily (volatile elements) may vaporize during the printing process, leaving behind tiny holes that contribute to lower density [60,61].

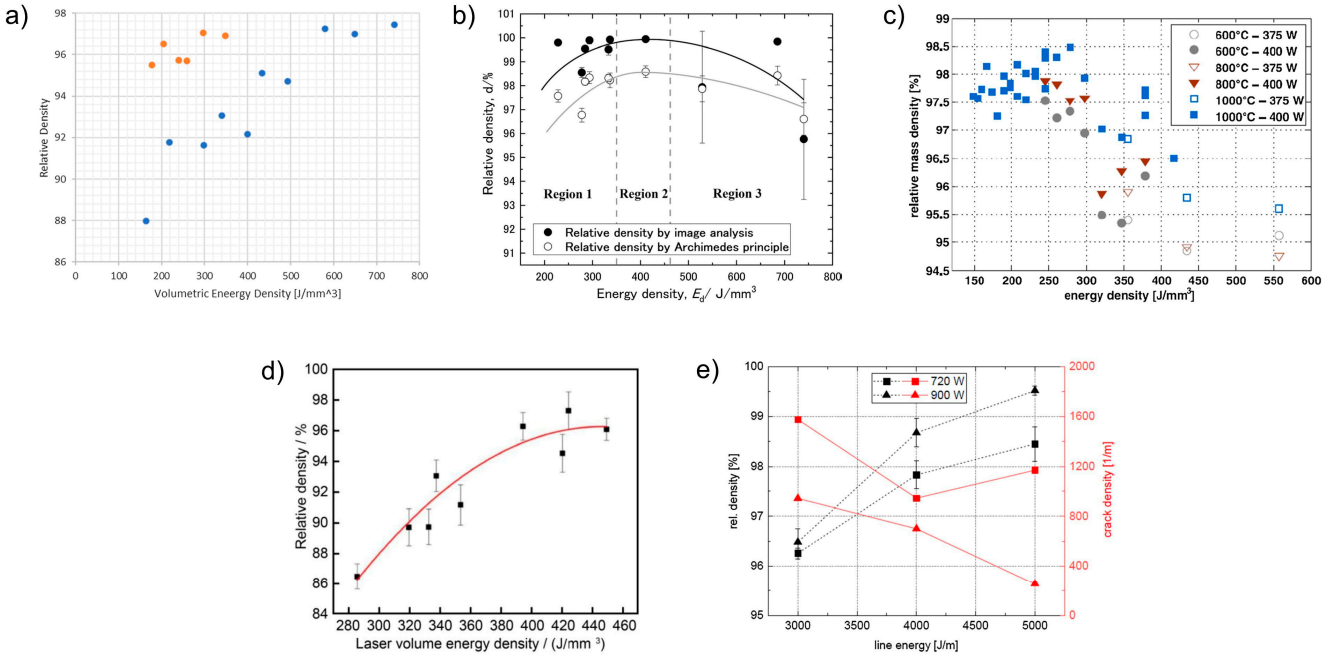

Figure 3. (**a**) The relative density of SLM-fabricated W cubes [36,108], (**b**) influence of VED on the density of pure W parts made with SLM [50], (**c**) influence of substrate preheating temperatures on the relative density of W samples [19], (**d**) relationship between VED and density in W-nickel alloy (W-15Ni) parts fabricated using DED [74], and (**e**) influence of LED and electron beam power on the relative density of W parts made with EBM [58]. Data and figures were reproduced with permission from Elsevier.

The work of Wang et al. on the laser-based DED processing of W found the relative density of fabricated parts increases with VED (Figure 3d) [74]. In their study on EBM processing of unalloyed W, Dorow-Gerspach et al. investigated the impact of LED variations by altering the power and speed of the electron beam to assess its effect on cubic samples [65]. These experiments were carried out at a substrate preheating temperature of 1000 °C. They achieved a high relative density of 99.5% but observed cracking in all fabricated cubes. While increasing electron beam energy led to a decrease in relative density, it also resulted in a decrease in crack density (Figure 3e), highlighting the trade-off between densification and structural integrity in this AM process [65].

High energy inputs in AM processes that include SLM affect the molten pool due to the Marangoni effect. The severity of this effect is directly proportional to the laser energy input [38,111,112]. This effect can drag gas into the molten pool, leading to pore formation upon solidification. Excessive laser energy density, especially at lower scan speeds, can also result in molten pool instabilities, yielding a rough track [29]. As SEM images showing the typical surface morphologies of scanning tracks at different laser powers in the AM processing of W (Figure 4a–e [29]) indicate, an optimal laser power can result in a regular flow front and no cracking (Figure 4b).

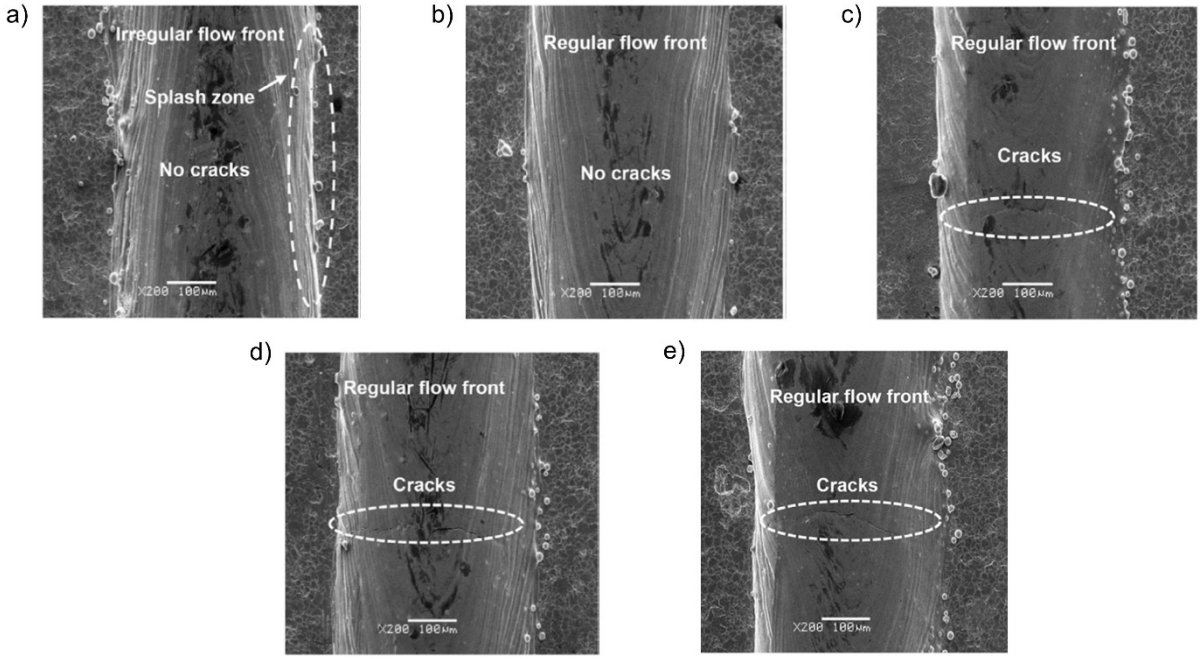

Figure 4. SEM images showing surface morphologies of scanning tracks at a laser power of (**a**) 250 W, (**b**) 300 W, (**c**) 350 W, (**d**) 400 W, and (**e**) 450 W; the scanning speed is 200 mm/s [29].

Properly controlling the melting behavior during AM can yield several significant advantages. High energy input facilitates the mixing of elements with lower melting points, enhancing interfacial bonding through Marangoni convection [29,97]. Stable molten pools promote the formation of complete columnar crystals in additively manufactured W parts [32]. Additionally, techniques such as EBM can introduce remelting during AM, annealing the built portion of the W parts, and reducing their susceptibility to cracking [63]. Another parameter affecting melting in AM processing is the layer thickness, as indicated in Equation (1). The comprehensive review by Marcos et al. indicates that reducing the layer thickness in PBF processes requires less energy to melt the powder, resulting in continuous conduction mode tracks at lower energy input levels [58].

Scan Speed

Scanning speed is a dominant factor, accounting for a ~75% variation in W densification within the SLM process [51,60]. Ren et al. [17] examined how the morphology of W single tracks can be influenced by laser power and scanning speed. These single tracks were printed onto a stainless steel substrate preheated to 200 °C. Establishing a processing map based on the surface characteristics of the single tracks (Figure 5a) allows different regions to be delineated, where one can observe regular tracks, irregular tracks, or instances of balling. The scanning speed plays a critical role in determining the quality of the fabricated tracks. At lower scanning speeds, the laser imparts sufficient energy to the powder, facilitating the formation of regular and continuous tracks. Conversely, as the scanning speed increases, the reduced time available for melting and consolidation leads to the formation of irregular tracks and balling, where molten material forms spherical particles instead of continuous lines.

Rebesan et al. [37] explored how adjusting the laser scanning speed and spacing between hatch spacing affects the density of SLM-fabricated W parts under Ar atmosphere at a power of 170 W and spherical particles (Figure 5b). This approach resulted in achieving high relative densities of 96.4% to 99.6%. Enneti et al. took a different approach, with the laser power kept at 90 watts, a VED of 1000 J/mm^3, and the base plate preheated to 80 °C [51,102]. With these settings, densities ranging from 60% to 75% were achieved. Li et al. [113] examined the impact of process parameters (laser power, scanning speed,

hatch spacing) on the density of as-SLM bulk W parts, achieving a maximum relative density of 98.31%, and creating process maps (Figure 6). Here, there was a direct correlation between laser power and density (Figure 6a), with hatch spacing and scanning speed having minor effects (Figure 6b,c). High densities (>98%) were consistently attained with 250–300 W power, 0.08–0.1 mm hatch spacing, and 0.03 mm layer thickness, offering valuable insights into process optimization. Xiong et al. [45] used image analysis to measure density and established process parameters for achieving high-density W coupons. They achieved densities of 97.3% to 98.1% with laser powers between 250 and 300 W and scanning speeds of 400 to 500 mm/s. Dong et al. [114] conducted a study to investigate how various factors influence the quality of AM-produced W parts. They utilized a preheating temperature of 100 °C and employed irregularly shaped (polyhedral) particles for the powder material. Furthermore, they observed that higher laser power and slower scanning speeds produced denser parts. However, when the scanning speed was excessively high, it caused the material to ball up and led to the formation of surface pores. Specific studies on the effect of nitrogen on W-AM are limited. Dong et al. [114] found that W parts printed under a nitrogen atmosphere achieved higher density, hardness, and overall strength compared to those printed under an argon atmosphere.

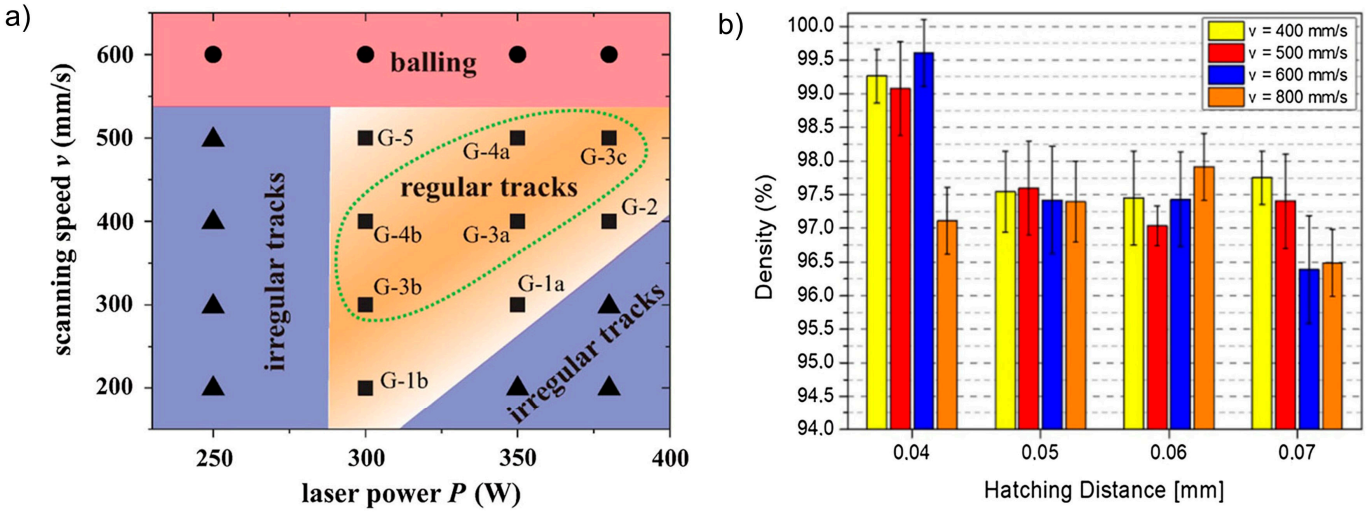

Figure 5. (**a**) Processing map for SLM of unalloyed W [17], and (**b**) the influence of hatch spacing and scanning speed on the relative density. The laser was maintained at a power of 170 W and the substrate was preheated to 80 °C [37]. Reproduced with permission from Elsevier.

Recent findings by Sharma et al. [98] have demonstrated a maximum relative density of 99.2% for pure W, which is the highest value reported in the SLM of pure W. They employed a multi-scale thermo-kinetic and thermo-mechanical computational model to fine-tune the laser parameters and understand the thermal behavior during the melting and solidification phases. Their work demonstrates the potential for further density improvement through controlling laser power, scan speed, and hatch spacing.

Other Scanning Variables and Strategies

The scanning pattern plays a critical role in determining the thermal history of processed W materials, offering flexibility suitable for a variety of applications. This flexibility represents a unique advantage of AM over traditional manufacturing techniques. Table 3 offers an overview of scanning variables and strategies employed in W-AM. The localized differences in material properties can be ascribed to the focused energy input from electron or laser beams or other energy sources that determine the thermal history experiences at a point [60]. In the EBM process, for example, one can witness multiple instances of melting and re-melting at a single scanning point [63]. EBM utilizes flexible bidirectional scan patterns to optimize densification and surface finish, leading to a high print quality [32].

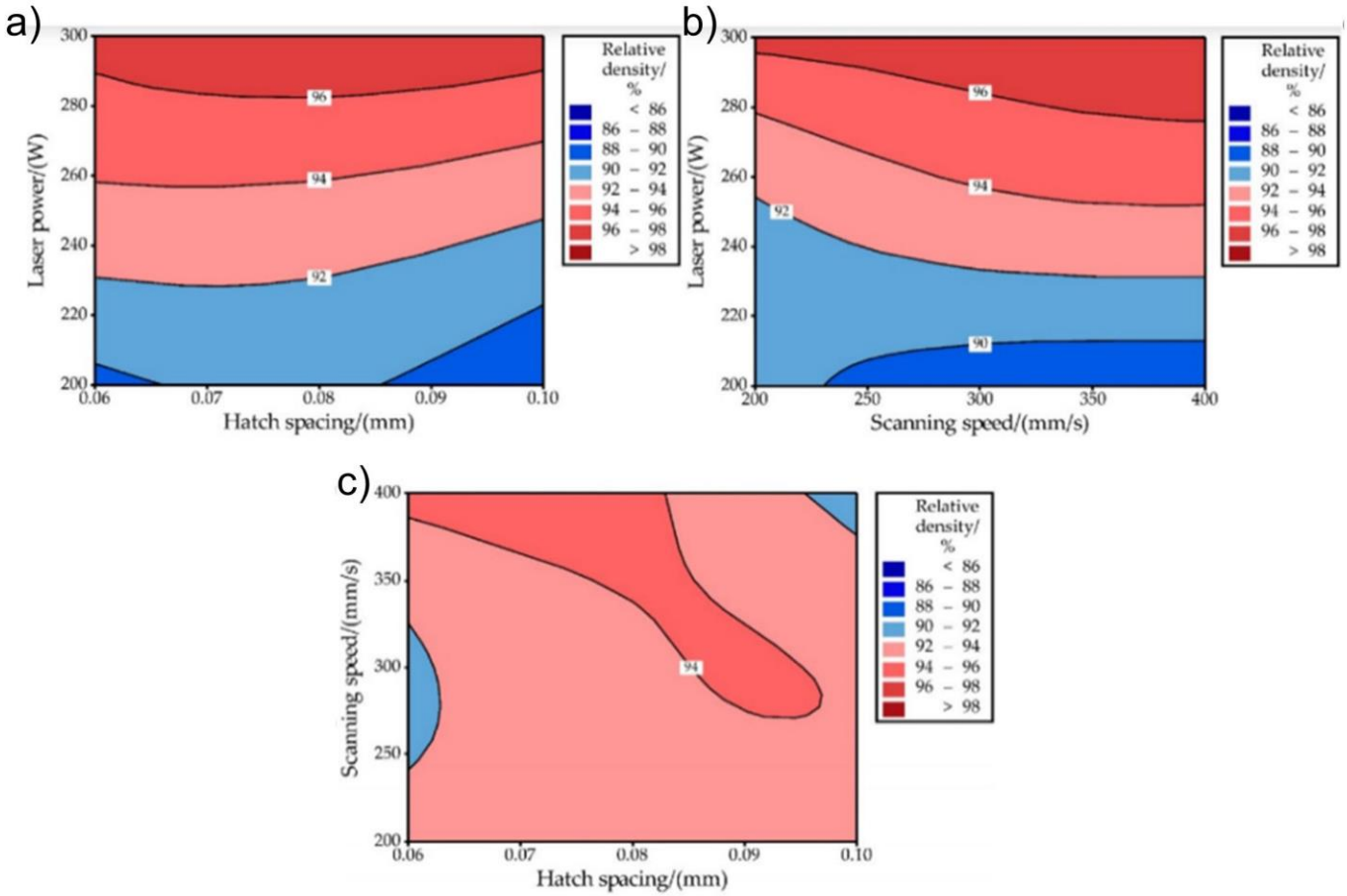

Figure 6. Processing map for SLM of W. (**a**) laser power vs. hatch spacing, (**b**) laser power vs. scanning speed, and (**c**) scanning speed vs. hatch spacing, [113].

In PBF for W materials, different scanning patterns have been explored. A 67° rotation between layers randomizes grain orientation, reducing the ladder-shaped grain structures which are potential crack-formation sites [21]. While many studies adopt a 67° rotation to minimize scan alignment, others use rotational angles of 45° or 90° [8,19,27]. Remelting, which is scanning a track multiple times before recoating, combined with rotation, curtails the formation of columnar grains and reduces longitudinal cracks, resulting in smaller grain sizes and reduced surface roughness [21,45,61]. Wang et al. [21] investigated crack development in SLM of unalloyed W. They studied three scanning strategies: parallel, 67° rotation, and remelting with 67° rotation. Matching scan tracks between layers resulted in consistent crack growth along the build direction. Rotation between layers reduced crack propagation, while remelting did not effectively reduce cracks but instead promoted thermal fatigue crack growth [21].

A growing body of research explores the relationship between scan pattern design and the properties of additively manufactured W materials. These studies have quantified the effects of specific pattern parameters. Hatch spacing, interestingly, is responsible for a mere ~7% fluctuation in the final W densification [60]. Point distance is another crucial factor in the AM relative density for W materials. Wang et al. [43] and Huang et al. [115] studied the influences of point distance and hatch spacing on the relative density of W achieved when pulsed (Figure 7a), and continuous lasers were used (Figure 7b,c), respectively. By adjusting these parameters, different melting strategies can be deployed, presenting an opportunity to oversee and regulate re-melting sequences to ensure that they sidestep randomness [46].

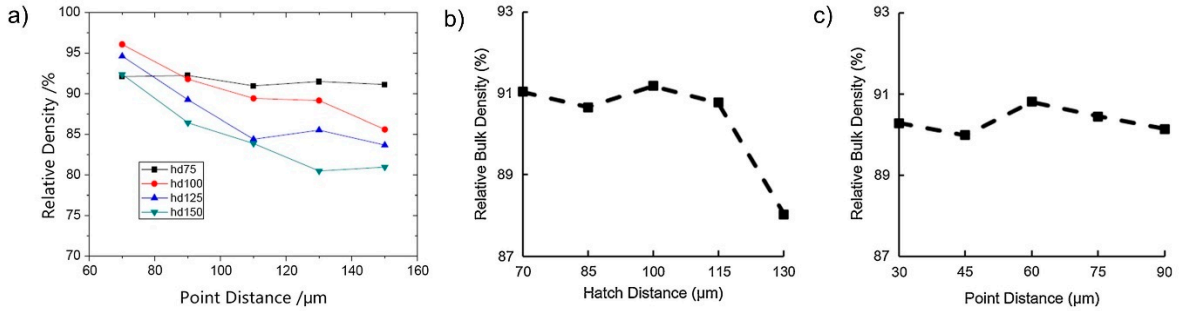

Figure 7. Influence on the relative density of manufactured W cubes due to the interaction between hatch spacing and point distance with input parameters of (**a**) a pulsed laser power of 400 W and exposure time of 100 μs [43], and (**b**,**c**) a laser power of 40 W, layer thickness of 50 μm, and exposure time of 300 μs [115]. Reproduced with permission from Elsevier.

In examining the role of scan track design, we find it plays an important role in pattern design, especially in upholding the quality of SLM-fabricated parts [60]. Parameters such as the single scan track width and hatch spacing can be adjusted. Within SLM, the overlap rate is devised in line with these two parameters, serving as an analytical tool to gauge conditions across multiple scan tracks. Previous studies have underscored a non-linear relationship between scan track characteristics, which is dictated by overlap design choices, and the eventual densification of W material. This points to the existence of an optimal overlap rate that balances these parameters [17].

Table 3. An overview of scanning variables and strategies employed in the AM of W.

Parameters	Details	Reference
VED	- **VED:** - ***Increased power*** in AM affects the molten pool via the Marangoni effect, with the severity proportional to laser energy. - Can introduce gas, causing pore formation and pool instabilities, resulting in rough tracks. - Enhances the densification of manufactured parts. - Reduces residual stresses via annealing. - Relates to pattern design. - ***Extremely high energy densities*** (>300 J/mm^3) have drawbacks: more porosity, excessive fusion risks, disrupted melt pools with stuck powder particles, and the vaporization of volatile elements. These challenges impact printed part quality. - ***Controlled melting has benefits,*** allows the mixing of low melting point elements, and improves interfacial bonding. It promotes the growth of full columnar crystals in W-AM.	[19,29,32,38,50,60,61,63,74,97,109–112]
Scanning Variables	- **Direction and Angle:** - EBM process allows multiple instances of melting and re-melting at a single scanning point. - 90° alternating bidirectional scanning in SLM. - 67° alternating bidirectional scan. - **Speed:** scanning speed affects ~75% of W densification variation in SLM. - **Hatch Spacing:** affects ~7% of W densification variation. - **Overlap Rate:** The relationship between scan track characteristics and final W material densification is non-linear. An optimal overlap rate exists. - **Scan Track Width**	[17,19,27,32,46,51,60,63]

Wetting Behavior and Interfacial Characteristics

For producing high-quality components via AM, interfacial design and W wetting behavior at multiple scales are vital due to their well-documented influence on reducing crack initiation and propagation, and on mechanical properties (Table 4). Microscopic wetting behavior involves the internal heterogeneous boundaries within the AM-produced W parts. W is not easily wettable by most metals at low temperatures (below 2000 °C). The temperature-dependent wettability of W has been a focal point for many researchers [60,116]. Muramatsu et al. [97,117] underscored the significance of the heterogeneous interface, especially when considering the broad temperature range covered in AM processes [97,116,118]. To enhance the AM quality of W-based materials, researchers have introduced small quantities of transition metals like Ni and Fe. These elements reduce the activation energy required during the sintering of W, accelerate W diffusion, and provide improved wettability to facilitate an AM process [60,97].

Table 4. An overview of W wetting behavior and interfacial phenomena at micro as well as macro scale in AM processes.

Category	Description	Examples and Developments	References
Microscopic Wetting Behavior	Concerns internal heterogeneous boundaries in W-AM.	- Temperature-dependent wettability of W - Introduction of Ni and Fe to improve wettability and AM quality	[60,97,116–118]
Macroscopic W Material/Substrate Interfacial Wetting and Reaction	Relates to interfaces between the substrate and W material, affecting parts quality.	- Use of stainless steel interlayers containing nickel - Substituting substrates with Ti-based alloys, e.g., Ti–6Al–4V - Sandwich-structural printing sequences - Risks of diffusion-induced secondary phases and unwanted reactions	[32,73,97,119]

On the other hand, macroscopic W material/substrate interfacial wetting and reaction involve the interfaces between the substrate and the W material to influence the final quality of an AM part. Stainless steel interlayers, containing nickel, have been employed to improve the adhesion between W and other alloying elements because of an enhanced solid-state diffusion and grain boundary diffusion [97]. For better outcomes, substrates can be substituted with Ti-based alloys such as Ti–6Al–4V due to the enhanced thermodynamic compatibility between W and Ti [32]. Novel approaches, like sandwich-structural printing sequences, have been developed for W materials, leading to better quality AM parts [119]. However, using such interlayers can lead to diffusion-induced secondary phases. Additionally, interactions with other elements might bring about unwanted reactions, such as the peritectic reaction seen between Fe and W during non-equilibrium solidification [73,97].

3.3. Oxygen, DBTT, and Micro-Cracking

Oxygen, along with other interstitial contaminants like nitrogen and hydrogen, presents serious challenges in the AM of refractory alloys (including W materials). Such contaminants, particularly oxygen, critically affect properties like the DBTT value in W materials, with molten W being especially sensitive to oxygen [17,120–122]. This heightened sensitivity leads to embrittlement, increasing DBTT, and decreased strength. Table 5 summarizes the current understanding of oxygen contamination for W in AM processing. Common sources of oxygen contamination include oxidized powder surfaces, residual oxygen in the chamber [49], and oxygen present in the substrate due to high thermal energy inputs which suggests that substrates may function as oxygen reservoirs [19]. The powders utilized in AM, owing to their vast surface-to-volume ratio, are notably prone to absorbing oxygen from their surroundings. Moreover, when W is exposed to oxygen at room temperature, it promptly forms an oxide layer within an hour [123]. Nagy and Humphry-Baker [122] conducted a study on the oxidation of W and developed a W oxidation mechanism map to reveal the kinetics of W oxidation at the 600–1600 °C temperature range (Figure 8).

This can be useful in W-AM. Under AM's elevated temperatures, oxygen can not only diffuse swiftly into the alloy but also react with W, resulting in intergranular cracking upon cooling [48,63,124].

Table 5. Current understanding of interstitial contamination in W during AM processing.

Factor/Parameter	Details/Effects	References
Contaminants	Oxygen, nitrogen, hydrogen	[17,120–122]
Adverse Effects	- Embrittlement - Shifts in DBTT - Strength reduction - Cause cracking especially at HAGBs	[17,21,120–122]
Sources of Oxygen in W Materials	- Oxidized powder surface - Residual oxygen in the chamber - Substrates due to high thermal energy inputs	[19,49]
Oxygen Sensitivity in W Materials	- Molten W is sensitive to oxygen - Oxide layer formation (1 nm thick within an hour) - Potential for intergranular cracking upon cooling	[48,63,123,124]
Oxygen Control Techniques in AM Processes	- Higher beam power - Enhanced VED - Radio frequency induction plasma treatment	[26,63]
Material Design for Reduced Oxygen Sensitivity	Introduction of alloying elements such as Ta to W	[48]
Important Studies and Findings	Oxidation mechanism map for AM applications exists	[122]

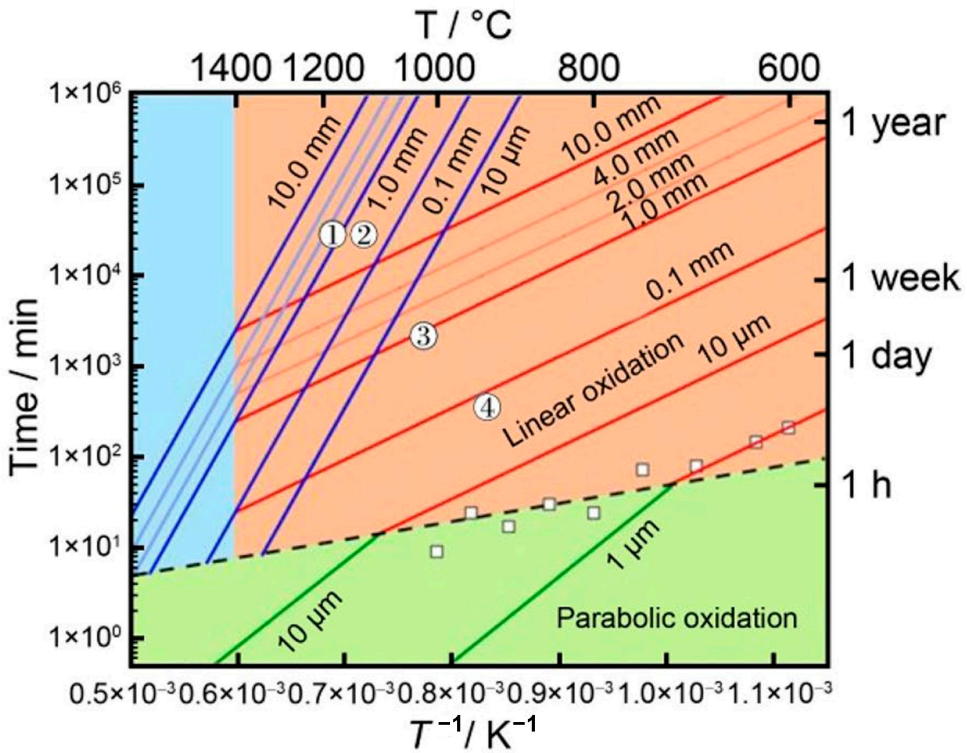

Figure 8. W oxidation map in the temperature range of 600–1600 °C and up to 2 years. Contours indicate the thickness of the metal oxidized. The parabolic, linear, and sublimation regions are shaded in green, red, and blue respectively [122]. Reproduced with permission from Elsevier.

Reducing oxygen levels during the AM process is paramount, as this will improve part quality by reducing the occurrence of cracks [49]. W oxides can remain stable at

up to 2000 °C, potentially initiating cracks during rapid solidification [120]. To confront these challenges, researchers can turn to several strategies in many metallic systems. Gas atomization under inert conditions delivers powders with appreciably lower oxygen and nitrogen contents. The use of inert gas environments, such as argon or helium, during AM offers a practical way to minimize contamination by isolating the alloy from potential contaminants. Additionally, enhancing powder handling and storage protocols—like the vacuum packaging of powders and handling under inert atmospheres—is another avenue being explored to eliminate contamination. Implementing techniques like using higher beam power and enhancing volumetric energy density can diminish the oxygen content and curb cracking [63]. The role of oxygen is not just restricted to the fabrication process but extends to preheating, underscoring the necessity for an oxygen-regulated environment [32]. Innovatively, as pointed out earlier, methods such as radio frequency induction plasma treatment have been deployed to manage oxygen levels effectively [26]. Furthermore, material design advancements, like introducing Ta to W, offer a promising avenue to counteract oxygen sensitivity [48]. To facilitate deeper insights, detailed studies to understand W oxidation have been undertaken, resulting in the creation of an oxidation mechanism map tailored for AM [122].

Crack nucleation and propagation in the AM of W correlate with its high DBTT of approximately 200–600 °C. Support for this comes from an observed delay between solidification and crack appearance using in situ high-speed cameras reported by Vrancken et al. [24,35]. Cracks often propagate along high-angle grain boundaries (HAGBs) [21], where the formation of cracks in the intergranular regions of SLM-fabricated W has been mostly observed. Such behavior is linked to W's grain boundary sensitivity to impurities, notably oxygen, found in amounts between 30 and 370 ppm in W powder [24,38]. While some researchers attribute cracks to W oxide aggregation during solidification [21,37,41,42], persistent cracks at low oxygen levels indicate other possible influencing factors as well [24]. The role of impurities, including oxygen and hydrogen, in SLM on W brittleness has not been fully explored. High-speed in situ SLM videos show cracking across W's DBTT, likely due to the increased stress [24]. Such stresses from SLM may only be offset by cracking at impurity-contaminated grain boundaries [42,125]. A study by Rebesan et al. on SLM-fabricated W specimens revealed a high cracking tendency [37]. Two types of cracks were identified: longitudinal (along the melt-pool center) and transverse (perpendicular to laser-induced surface ripples). Longitudinal cracks are linear and 30–100 μm long, while transverse cracks are shorter with an "S"-shape along grain boundaries (Figure 9). The extensive cracking results from thermal stresses during rapid solidification or recrystallization (Figure 10a), particularly below the DBTT. Micro-cracks that resemble intergranular hot cracking form due to nanopore aggregation at grain boundaries induced by boiling W oxides (WO_x) in the melting pool (Figure 10b) [37].

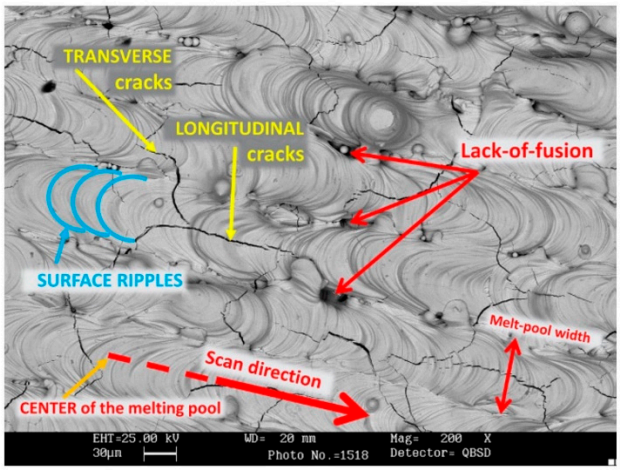

Figure 9. SEM image of surface morphology and crack type in SLM-fabricated W [37].

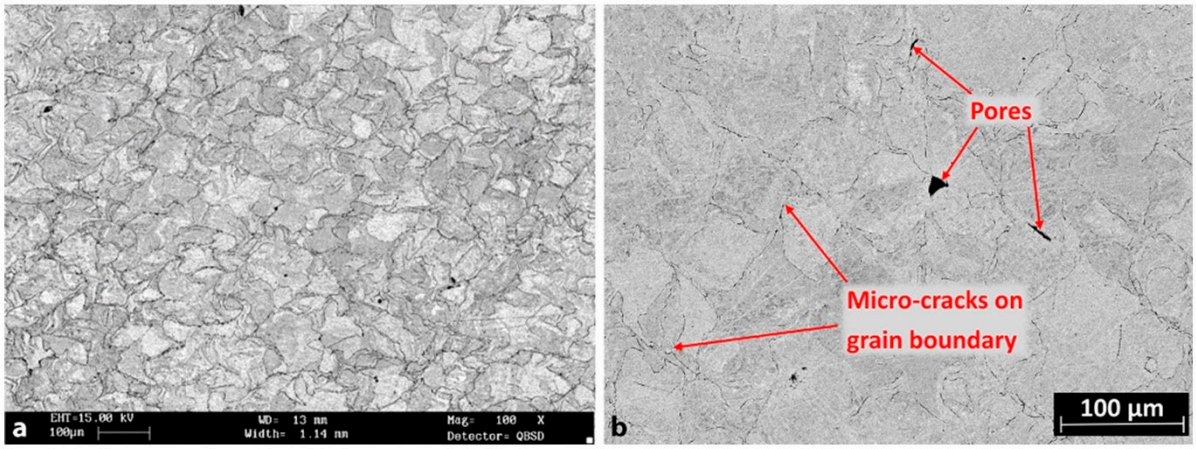

Figure 10. SEM images of SLM-fabricated W sample, (**a**) electrolytically etched displaying a crack network; (**b**) a higher magnification of grain boundaries displaying micro-cracks and pores [37].

Cracking in EBM-produced W is comparable to in an SLM one, with their mechanisms still under debate. Solid-state cracks may arise from inelastic deformation near low-angle grain boundaries (LAGBs) (Figure 11a), which is supported by EBSD data (Figure 11b) [63]. In laser-based DED, residual stress-induced cracking due to high thermal gradients and porosity are common challenges [61]. Oxygen contamination and its contribution to micro-cracking is another challenge.

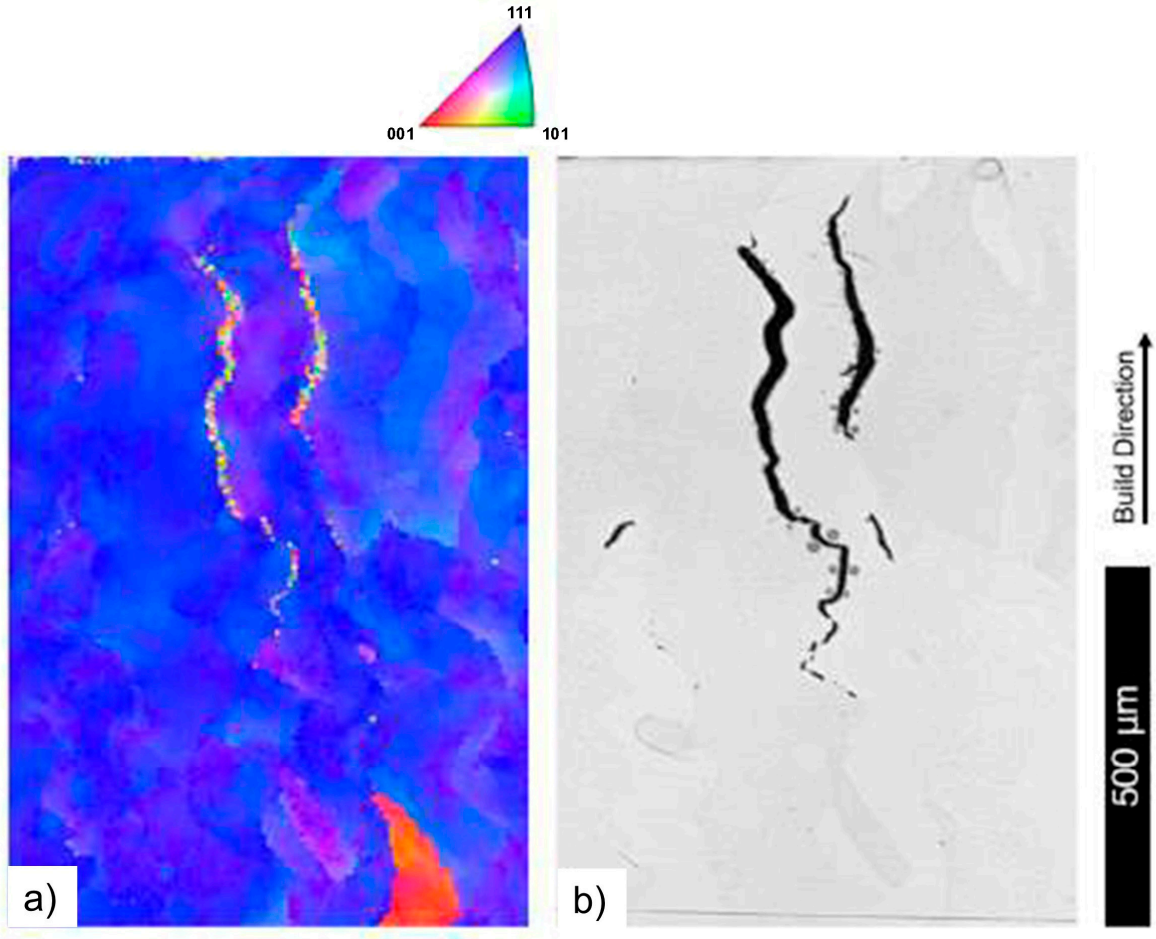

Figure 11. A vertical crack at grain boundaries of EBM-fabricated W samples: (**a**) EBSD in which the crack appears as random unindexed pixels, and (**b**) an optical image [63].

Overall, micro-cracking in W-based alloys arises due to several mechanisms, which are as follows. Thermal stress: The high melting point and low thermal expansion coefficient of W lead to substantial thermal gradients during the rapid heating and cooling cycles in AM processes. These thermal gradients induce thermal stresses that exceed the material's fracture toughness, resulting in micro-cracks. Solidification cracking: During the rapid solidification in AM, the difference in cooling rates can cause uneven shrinkage and create tensile stresses in the material. If the material solidifies with significant residual stresses, it can lead to solidification cracking. The presence of impurities and alloying elements can intensify this issue by creating brittle phases or weakening grain boundaries. Phase transformations: Certain tungsten-based alloys undergo phase transformations during the cooling process. These transformations can involve volume changes that induce additional stresses within the microstructure, contributing to micro-cracking. The incompatibility between different phases in terms of their mechanical properties can further complicate this problem. Porosity and defects: Incomplete melting and impurities can introduce porosity and other defects within the material. These defects act as stress concentrators and can initiate micro-cracks under the applied thermal and mechanical loads during the AM process and subsequent cooling. Grain boundary embrittlement: Alloying elements or impurities that segregate to grain boundaries can weaken these boundaries and make them more susceptible to cracking under thermal and mechanical stresses. This embrittlement can significantly contribute to the formation and propagation of micro-cracks. In addition to powder and process parameter-related solutions, post-processing techniques like hot isostatic pressing (HIP) can be explored as viable techniques for closing microcracks in W-based alloys to enhance the overall mechanical properties of AM-fabricated W components.

Substrate Preheating

Utilizing a heated substrate plate in PBF processes can potentially mitigate the problems posed by thermal gradients [19,38]. Preheating is an essential preparatory technique implemented before the actual PBF processes to optimize the material's structure and improve the resultant properties. This method confers several advantages (Table 6). Firstly, preheating aids in the mitigation of built-up thermal residual stresses within the material to enhance its stability [109]. Moreover, by controlling the melt pool's cooling rate and the thermal gradient during solidification, preheating ensures improved material formation and properties. This is particularly critical for W which has a high DBTT; preheating can potentially delay or even avert this transition [44]. Additionally, preheating can emulate the annealing process, refining W's microstructure to produce parts with increased density and fewer microcracks [109]. In some cases, preheating the substrate to temperatures close to 1000 °C has proven effective in achieving those outcomes [19].

Elevating substrate temperature beyond W's DBTT decreases cracking likelihood, thereby improving the relative density of parts manufactured using AM with W. SLM processing at increased temperatures from 200 °C to 1000 °C reduced cracking. Such findings have been visually represented in the works of Muller et al. (Figure 12) [19], where they compare the microstructure of SLM-fabricated W with a substrate temperature of 200 °C that includes grain boundary cracks (Figure 12a) to that of a SLM-fabricated W using a substrate temperature of 1000 °C without cracks (Figure 12b). In another study, using ~850 °C substrate heating led to minor cracking [32]. Other observations indicate that temperatures below 400 °C are inadequate for preventing microcrack formation [8]. Vrancken et al. also showed that the exact temperature above which cracks in SLM-fabricated W are eliminated ranged from 500 °C to 600 °C. The crack-mitigating effect of preheating persists when scaling up from a single scan track to a hatched area. Without preheating, a large crack network is formed (Figure 13a), whereas only small, isolated cracks are found using 500 °C preheating (Figure 13b) [44].

Table 6. An overview of the effects and benefits of preheating in the AM of W materials.

Preheating Effects		Information/Description	Reference
Purpose		Used before the process to enhance obtained properties	
Benefits			
-	Mitigation of Stress	Reduces built-up thermal stresses	[102]
-	Melt Pool Dynamics	Controls cooling rate and thermal gradient during solidification	
-	Delay/Avoidance of DBTT	Delays or prevents DBTT	[44]
-	Annealing Effect	Simulates the annealing process, refining W microstructure	[109]
-	Enhanced Density and Reduced Microcracks	Increases part density and reduces microcrack formation, especially with preheating up to 1000 °C in SLM, and more in EBM	[19,63]
Optimal Preheating Range			
-	Observation	Low preheating temperatures below 400 °C are insufficient for microcrack mitigation of W materials	[8,32]
-	General Findings	Higher preheating temperatures minimize high DBTT effects and enhance the density of W parts	[19]
Drawbacks of Excessive Preheating			
-	Recrystallization	Extremely high temperatures trigger recrystallization in material	[63]
-	Grain Vulnerabilities	Larger recrystallized grains are prone to intergranular cracking, acting as pathways for cracks near grain boundaries	[60,121]

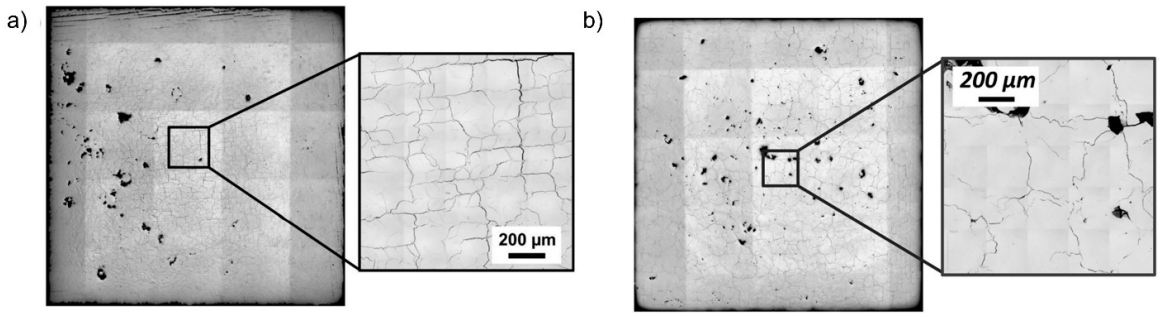

Figure 12. Effect of temperature on SLM-fabricated pure W cubes: (**a**) optical image of a cross-section at 200 °C, (**b**) optical image of a cross-section at 1000 °C [19]. Reproduced with permission from Elsevier.

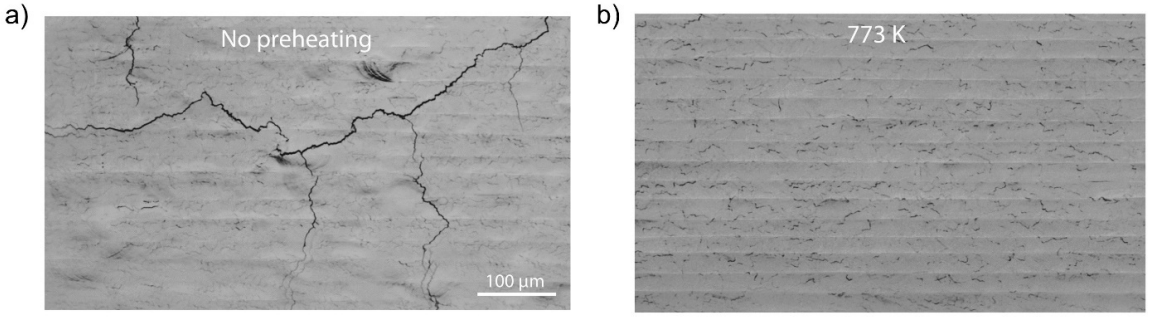

Figure 13. Crack formations in SLM-fabricated W samples: (**a**) crack pattern of a 1 by 2 mm area scanned using hatch spacing h = 25 µm, and (**b**) absence of cracks in a 1 by 2 mm area scanned using 500 °C preheating [44]. Reproduced with permission from Elsevier.

In EBM processing of W, preheating each layer up to 1800 °C may be required to fabricate high density parts [100]. Ellis et al. observed a lower crack density at 1500 °C

(corresponding to a preheating input energy of 735 J/mm^2) than at 1100 °C (corresponding to a preheating energy input of 325 J/mm^2), as shown in Figure 14a,b [63]. This led them to postulate that the higher preheat energy suppresses cracking by raising the ambient temperature of the build [63]. While preheating is beneficial, overdoing it can have detrimental effects. Excessive preheating temperatures can induce undesirable recrystallization processes within W materials [63]. The formation of larger recrystallized grains, a consequence of intense preheating, makes the material susceptible to intergranular cracking [60,121]. These grains can then become crack-initiation points, especially in regions close to or on the grain boundaries [60,121]. As a result, extremely high preheating temperatures can be counterintuitive and diminish the quality of the product [63].

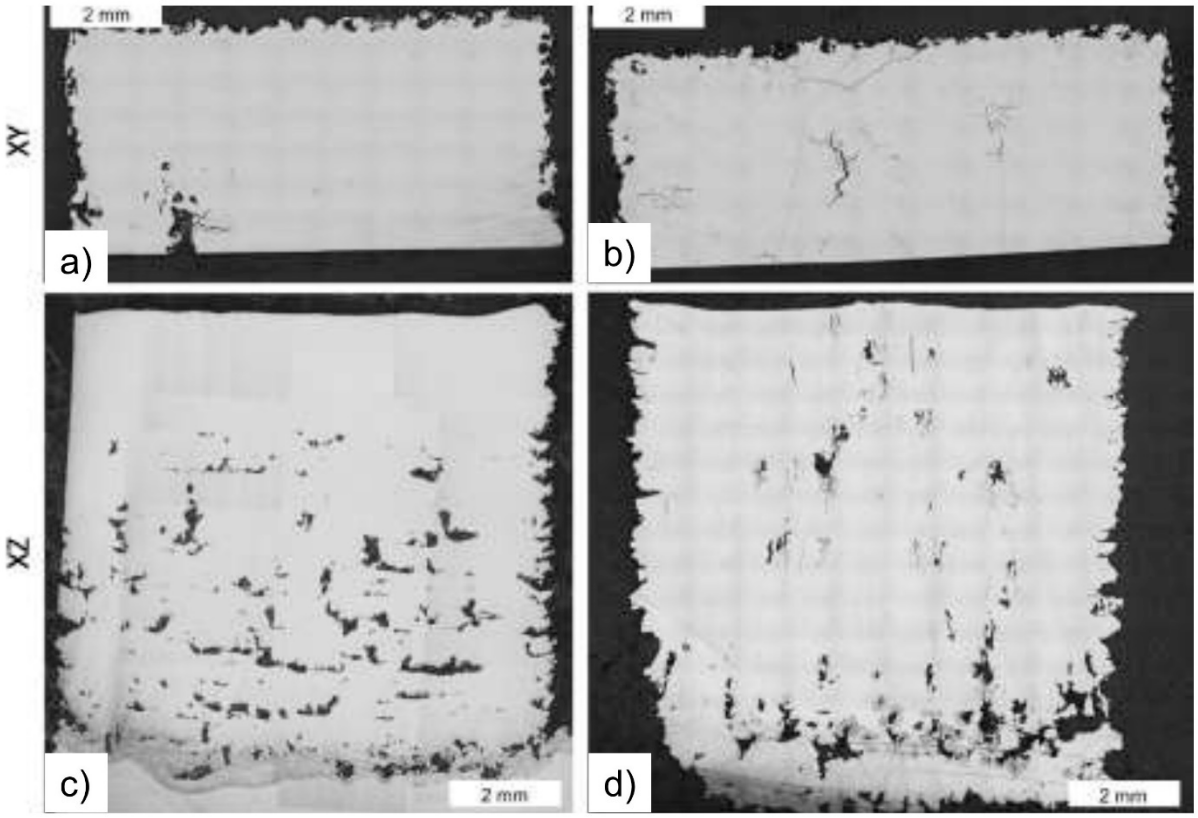

Figure 14. Cracking in EBM-fabricated W blocks built with nominally identical melt parameters: (**a**,**b**) XY sections, approximate elevations 9 mm, (**c**,**d**) XZ sections, approximately at the midline. The build shown in (**a**,**c**) did not crack; the build in (**b**,**d**) exhibited cracking [63].

Residual stresses in W-AM arise from W's high melting point and low thermal expansion coefficient. These stresses are generated by the complex thermal cycles experienced during AM processes, including thermal gradients, solidification stresses, phase transformations, and mechanical constraints. W parts undergo rapid heating and cooling, leading to steep thermal gradients that cause differential expansion and contraction. This results in tensile and compressive stresses within different regions of the part. Furthermore, as the molten W solidifies, the material shrinks. Non-uniform solidification and cooling rates across the part introduce residual stresses due to uneven shrinkage. Additionally, W-based materials may experience phase transformations during cooling, involving volume changes that generate further stresses. The build platform and surrounding material can also constrain the part, leading to residual stresses as the material contracts upon cooling. Mitigation strategies involve controlled cooling post-deposition to minimize thermal stresses through preheating, optimizing scan strategies, and designing effective support structures.

Thermal management is crucial in W-AM and can be addressed through various strategies during the design, AM processing, and post-AM processes. Enhanced support

structures specifically designed for W-AM can effectively dissipate heat and stabilize the part. Preheating the build platform, optimizing scan strategies, and adjusting process parameters to control cooling rates help maintain a more uniform temperature distribution, thereby reducing thermal gradients during the build cycle. Post-processing heat treatments, such as annealing or HIP, are employed to relieve residual stresses and improve the microstructural integrity of AM-produced W components, significantly reducing internal stresses and enhancing mechanical properties.

Ledford et al. [100] employed a comprehensive experimental design to establish an optimal processing window for achieving high-density, crack-free pure W using the EBM method. They successfully attained full density in select fabricated samples by preheating the substrate to 1800 °C and optimizing the other parameters such as scan speed and layer thickness. The as-fabricated W samples exhibited subgrains approximately 10–20 µm in size, with low-angle grain boundaries characterized by high dislocation densities ranging from approximately 1015 to 1016 per square meter in certain instances. High-temperature tensile testing revealed significant tensile anisotropy attributed to inherent crystallographic variations. Yield strength ranged from 85 to 202 MPa, while tensile strength ranged from 121 to 274 MPa, closely resembling annealed tungsten properties.

Similarly, Antusch et al. [126] utilized EBM to manufacture pure W components for nuclear fusion reactors, achieving 99.8% density and a crack-free microstructure characterized by elongated columnar grains. The absence of microcracks was attributed to reduced thermal stress facilitated by optimized pre-heating strategies during EBM and the absence of oxide precipitates due to manufacturing in a vacuum environment. This resulted in a stable melt pool during the fabrication process. Tensile testing conducted between 600 °C and 1000 °C demonstrated ductile behavior with a total elongation of 80% along the building direction and DBTT ranging from 700 °C to 900 °C. Thermal conductivity measurements were comparable with values in the literature for conventionally produced W counterparts. These studies highlight the potential of EBM as a promising method for processing W (Figure 15).

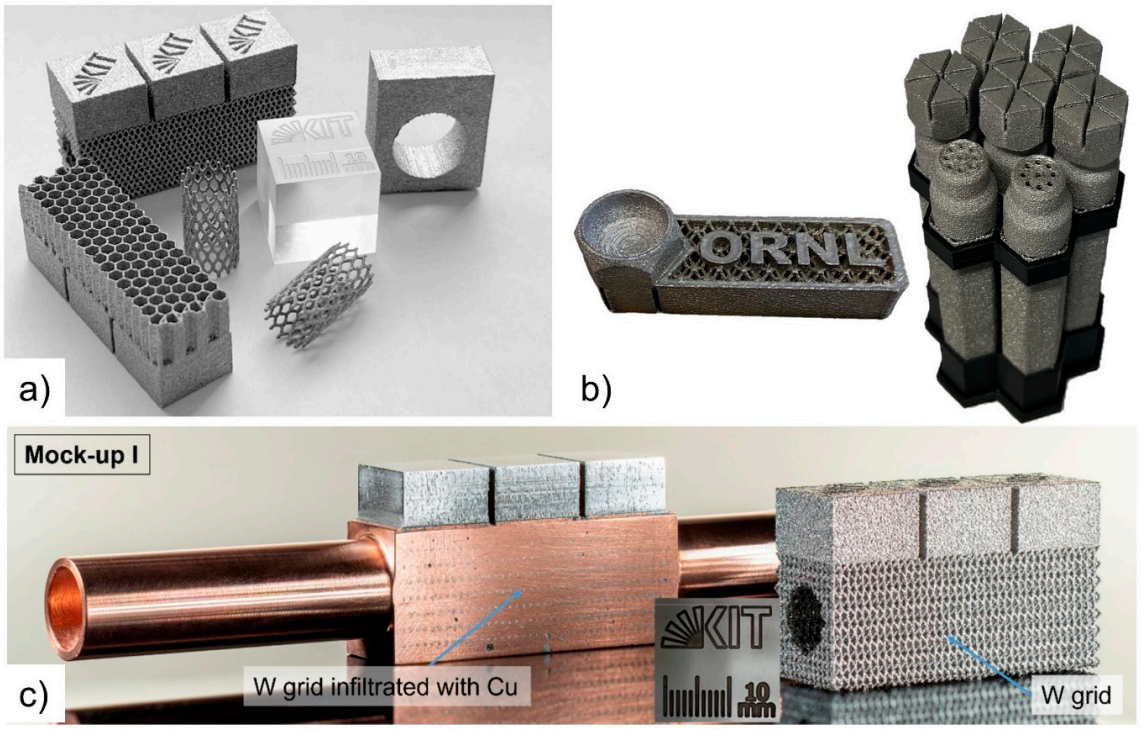

Figure 15. Pure W components fabricated using EBM: (**a**) complex geometrical parts [126], (**b**) a diverter tile and mesh demonstration piece, along with a mockup illustrating the potential diverter geometry featuring tungsten plasma-facing tiles [100], and (**c**) the integration of W-EBM with copper infiltration tailored for fusion applications [126].

4. Additively Manufactured W Alloys and Composites

Amongst the strategies to mitigate the challenges discussed in the preceding sections, alloying is a particularly useful approach. Alloying has been shown to impart multifaceted effects on the properties and behavior of W in AM contexts. Several W alloys have been studied in the realm of AM. Since W is often insoluble or immiscible with other elements, its alloyed materials with some elements, have been referred to as composites in some studies. In this review, we consider all combinations of W with other elements as alloys and refer to combinations of W with ceramic materials (such as carbides and oxides) as composites (Table 7). The AM-fabricated alloy groups that have been studied include W-Re [127–129], W-Ni [74,130], W-Ni-Fe [71,72,75,77,80,83,85,103,131–133], W-Ni-Fe-Co [134], W-Ni-Fe-Cu [80], W-Ni-Cu [4,135], W-Cu [4,6,136–138], W-Cu-Sn [139], W-Ta [8,140–143], W-Ta-Re [144,145], W-Nb [110], W-Fe [73,146], W-Mo [147], and W-Cr [86]. W-based matrix composites with different ceramic phases such as TiC [148,149], ZrC [120], TaC [150], La_2O_3 [44], CeO_2 [44], a mix of La_2O_3–ZrO_2–Y_2O_3 [44], and Y_2O_3 [42,61] have also been fabricated via AM methods.

Table 7. Additively manufactured W-based alloys and W-matrix composites.

Materials	References
W Alloys	
W-1–25%Re	[128,151]
W-0.1–40%Ni	[74,130]
W-7%Ni-3%Fe	[71,72,75,77,80,83,85,103,131,132]
W-4.6%Ni-2.4%Fe	[133]
W-6%Ni-2%Fe-2%Co	[134]
W-12%Ni-4%Fe-4%Co	[134]
W-18%Ni-6%Fe-6%Co	[134]
W-8.7%(Ni-Fe-Cu)	[80]
W-5%Ni-15%Cu	[3]
W-5%Ni-25%Cu	[135]
W-10%Ni-10%Cu	[135]
W-10–40%Cu	[4,6,136–138]
W-20%($Cu_{10}Sn$)	[139]
W-1–12%Ta	[8,140–143]
W-14.8%Ta-17.2%Re	[144,145]
W-5%Nb	[110]
W-14–79%Fe	[73,146]
W-50%Mo	[147]
W-12.85%Cr	[86]
W Matrix Composites	
W-0.5–2.5%TiC	[148,149]
W-0.5%ZrC	[120]
W-5%TaC	[150]
W-5%La_2O_3	[44]
W-2%CeO_2	[44]
W-1.75%La_2O_3-0.12%ZrO_2-0.12%Y_2O_3	[44]
Y_2O_3	[42,61]

A comprehensive review of the impact of alloying elements and ceramic particles on mitigating the challenges associated with the AM of W-based materials, as well as their microstructure and mechanical properties (Table 8), reveals several key purposes for these additions. Alloying elements and ceramic particles are introduced for the following purposes: to lower the melting point of W to enhance densification, for the modification of laser absorption, reduction in thermal conductivity of W, and reduction in melt viscosity to enhance densification, to form binding phases to enhance densification, improve grain boundary strengthening, modify grain structure, enhance grain boundary cohesion and improve pore distribution to enhance mechanical properties and to mitigate microcracking, to strengthen through secondary dispersed or precipitated phases to restrict grain boundary

movement and enhance mechanical properties to mitigate microcracking and enhance low-temperature ductility, increasing stacking fault energy, boosting dislocation mobility to improve ductility and lower DBTT, and for other purposes such as self-passivating behavior and the reduction in fuzz formation in the nuclear application.

Table 8. An overview of the impact of alloying elements and dispersion particles on mitigating the challenges of the AM of W-based materials and on their microstructure and mechanical properties.

Effects on W-AM	Alloying Element(s)	Specifics/Notes	Ref
Enhanced Densification	Ni, Fe, Co, Mo, Re, Ta, etc.	Due to the lower melting points of alloying phases densification is promoted. The melting of Ni, Fe, and Co enhances the dissolution of W particles.	[19,41,74,86,130,134–138]
	Cu	Occurs due to the role of alloying elements in forming binding phases. Good wetting allows the molten Cu to spread and adhere strongly to the W particles. Surface smoothing also contributes to a denser final structure.	[4,6]
	Ni, Cu, Ta, Fe, Mo	Modifications in laser absorption, melt viscosity, and fluidity. Ni works better than Cu. Ta increases recrystallization temperature and decreases thermal conductivity of WNi and Fe for improves wettability of W.	[4,6,8,74,130,135–138,140–143]
Microcrack Mitigation	Re, Ta, Nb, Mo, Cr, Ti, Ir	Re lowers the DBTT of W alloys, significantly reducing their tendency to crack during AM processes. Ta forms a special cellular structure that keeps tiny air pockets (nanopores) separated from each other. This reduces the overall tendency of the material to crack. Ta also oxidizes more easily than W during the building process. As a result, fewer nanopores form in the final W alloy, and the risk of microcracks is reduced. Nb improves the intergranular bonding of the alloy via solid solution strengthening. Cr forms the Cr-rich Cr-W phase and causes grain refinement. Ti (in conventional manufacturing of W) gives rise to a heterogeneous chemical distribution to prevent the nanostructured microstructure from coarsening. Ir (proved in conventional manufacturing of W) strengthens grain boundary cohesion, optimizes dislocation mobility, and reduces cracking. Adding some of these elements prevents the formation of tiny cracks (microcracks) in the building process. In general, W solidifies first, causing stress within the material. Alloying elements helps lessen this stress by essentially acting as a buffer. They also result in grain refinement of W, improved grain boundary strengthening, modified grain structure, and better pore distribution.	[4,44,48,86,110,127–129,141–144,152,153]
	Re	W, when alloyed with Re, showed a reduced DBTT and increased low-temperature ductility. This improvement is attributed to Re's high solubility in W and its capability as a solution hardener. The other benefits include the enhancement of grain boundary cohesion, boosting dislocation mobility and lowering DBTT, and reducing embrittlement.	[127–129]
	TiC, ZrC, TaC, Y_2O_3, La_2O_3, etc.	Y_2O_3 leads to more LAGBs and reduces cracking. W–Y_2O_3 has a better low-temperature ductility and suppresses cracking. La_2O_3 not only bolsters radiation resistance but also provides an indirect solution to these interstitial contamination challenges. ZrC nanoparticles decrease crack density due to finer grains and increased grain-boundary length. They also capture oxygen to form ZrO_y, reducing embrittlement. TaC supports the formation of W_2C phases within the material, further increasing the overall strength and crack resistance. It also reacts with any oxygen present, forming TaO_x, effectively removing oxygen from the system. TiC enhances hardness.	[42,47,120,141,150]
Mechanical Properties Adjustments	Fe	Strengthening by the formation of secondary or precipitated phases during AM processes. The non-equilibrium solidification between Fe and W allows for the potential formation of intermetallic phases like Fe_7W_6 and Fe_2W, improving the hardness.	[73,144,146]
	Ni	Tensile strength and fracture toughness enhancement.	[74,130]
	Ti, Ir, Hf	Increase in recrystallization temperatures. Potent carbide formers mitigate the adverse effects of carbon impurities on the alloy's mechanics. Elevate the recrystallization temperatures and improve W's low-temperature ductility and high-temperature strength. Ir can improve mechanical properties by increasing grain boundary cohesion.	[152–156]
	Ta, Nb, and other group V and IV transition metals	Improvement of intrinsic ductility of W alloys. Ta can increase hardness. Solid solution strengthening by Nb.	[110,141–144]
Others	Ta	Fuzz formation reduction, especially during He plasma irradiation.	[140]
	Cr and Y	Self-passivation behavior for high-temperature applications.	[157]

In the subsequent sections, we will closely examine some of these alloying strategies.

4.1. Alloying for Enhanced Densification

Alloying with metals that have lower melting points is a strategy to decrease the overall melting point of W. But it is important for this to be carried out in moderation to

ensure that the intrinsic high-temperature properties of the W alloys are retained [19,41]. W alloys behave differently when melted compared to pure W. The alloying elements can form phases with lower melting points than pure W, aiding in the binding and dissolution of W particles [4]. These elements can also affect melt viscosity and fluidity during AM, especially in SLM. Alloying elements can lead to unique solidification behaviors, leading to improved grain structures, and reduced stresses, among other benefits. Overall, W alloys generally exhibit superior AM part quality compared to the use of pure W [60,61]. A major consequence observed is the enhanced densification of the W matrix. Most alloying elements, including Ni, Fe, Co, Cu, and Re contribute to this phenomenon. The basis for this enhanced densification is the lower melting points of these alloying elements compared to W and the possibility of melting at lower energy inputs and faster scan rates. In the context of the SLM technique, the melting of Ni, Fe, and Co has been noted to expedite the dissolution of W particles [134,135], leading to a more consolidated alloy [6,130,134,135]. Cu, as an alloying element, has been studied to reveal its distinct role in W densification during AM [4,6,136–138]. The significance of Cu lies in its ability to form binding phases with W. The molten state of Cu ensures the effective wetting of W particles, while W particles concurrently undergo surface smoothing. Both these effects foster the increased densification of the W-Cu composite [4].

The alloying elements Ni, Cu, and Ta introduce significant changes in the AM process by altering parameters such as laser absorption, melt viscosity, and fluidity [4,6,8,74,130,135–138,140–143]. Among these alloying elements, Ni demonstrates superior efficacy over Cu in such modifications, primarily due to its lower thermal conductivity [42]. The use of Ta comes with its benefits, including the elevation of the recrystallization temperature and a decrement in thermal conductivity [4,130]. Re plays a multifaceted role in the AM of W alloys, one of which is its contribution to densification. The addition of Re allows for parts with higher relative density to be achieved (relative to pure W) (Figure 16a) [127]. The addition of alloying elements such as Cu, Ni, Fe, Mo, and Cr can facilitate higher densification in AM W materials (Figure 16b). Obtaining a relative density of more than 95% in SLM-fabricated unalloyed W is usually difficult, but precise scanning parameter adjustments, preheating, and the use of optimized starting materials have resulted in achieving relative densities over 98%. The EBM technique for unalloyed W fabrication has been shown to achieve relative densities up to 99.5%.

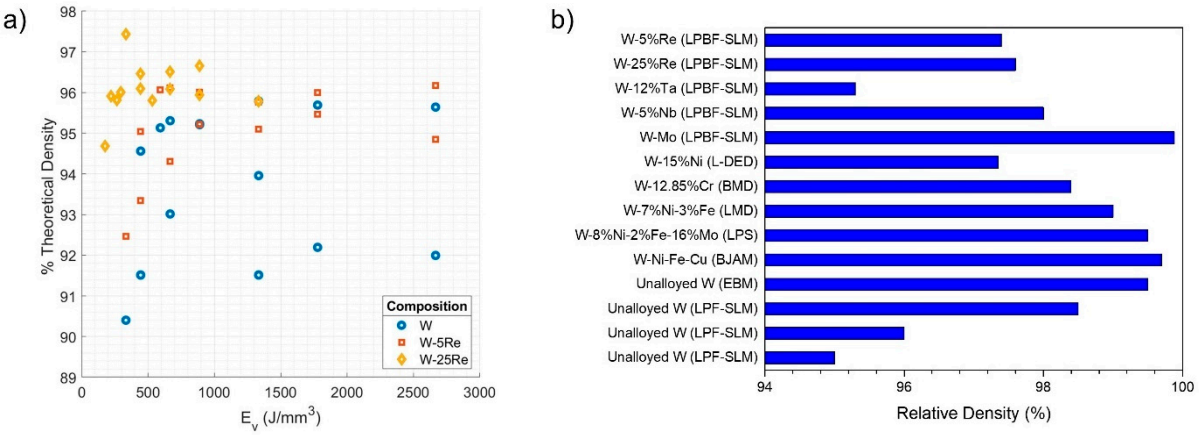

Figure 16. (**a**) Achieved relative (% of theoretical) desnity for SLM-manufactured W-5%Re, W-25%Re alloys, and unalloyed W versus energy density [127], and (**b**) obtained relative density of alloyed and unalloyed W fabricated via different AM techniques.

4.2. Alloying and Ceramic Dispersions for Microcrack Mitigation

4.2.1. Alloying Elements

Alloying is a very useful strategy for reducing interstitial contamination. The introduction of specific alloying elements in W during AM has been shown to substantially

impact the microcrack mitigation process, which is achieved through mechanisms such as grain structure modification, improved pore distribution, grain boundary strengthening, stress reduction, a decrease in DBTT, and reduced nanopore formation. The addition of Ta induces a cellular structure that spreads the nanopore distribution, culminating in an 80% reduction in cracking [48,143] (Figure 17). Furthermore, the role of Ta in reducing oxygen sensitivity during solidification, courtesy of its in situ oxidation, is essential in alleviating microcracks in the W alloy [48,141–143].

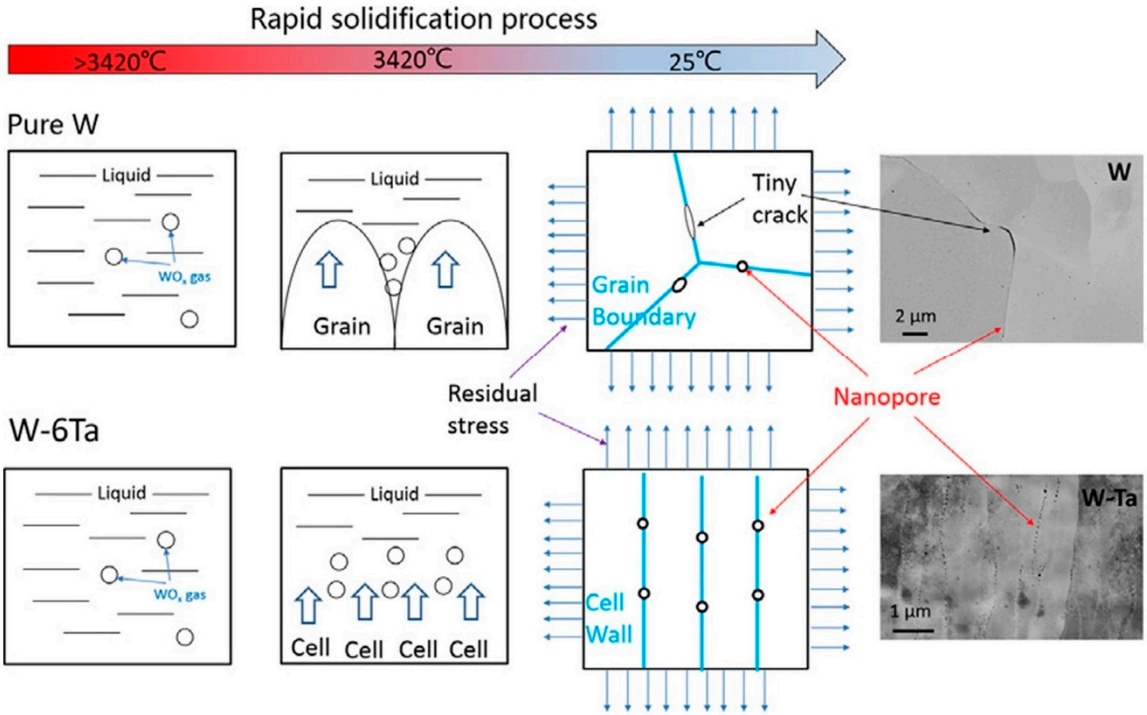

Figure 17. Schematic illustration of how adding Ta affects the formation of nanopores during SLM of W and W-Ta alloys [48].

Nb is beneficial as an alloying element due to solid solution strengthening, which strengthens intergranular bonding to provide an effective countermeasure against microcracking [110]. Alloying W with Re offers promising outcomes. Apart from its contribution to enhancing densification, the resultant alloys show enhanced grain boundary cohesion and an increased mobility of screw dislocations, significantly altering their mechanical behaviors. The addition of Re significantly reduces the ease at which W alloy cracks during the manufacturing process due to the significant lowering of the DBTT [127–129]. Eckley et al. [127] used EBSD maps and optical microscopy images to show significant cracking in pure W parts fabricated by SLM (Figure 18). Cracking increased with density and followed scan tracks, branching at 45-degree angles, and longitudinal cracking traced columnar grain boundaries in the build direction (Figure 18a,b). The introduction of 5 wt.% Re failed to effectively mitigate the observed cracking (Figure 18c,d). However, an increase in Re content to 25 wt.% resulted in a significant reduction in both surface and longitudinal cracking, and the characteristic horizontal and 45-degree angle cracking behaviors were notably minimized (Figure 18e,f). This improvement can be attributed to the lowered DBTT of W due to Re alloying, decreasing brittleness during cooling. Despite these enhancements, some cracking persisted. This study shows Re alloying to be effective in enhancing the crack resistance of W-AM. Notably, conventional fabrication has demonstrated the profound influence of Re, with W alloys containing 26 wt.% Re exhibiting a DBTT as low as −101 °C [60,155,156].

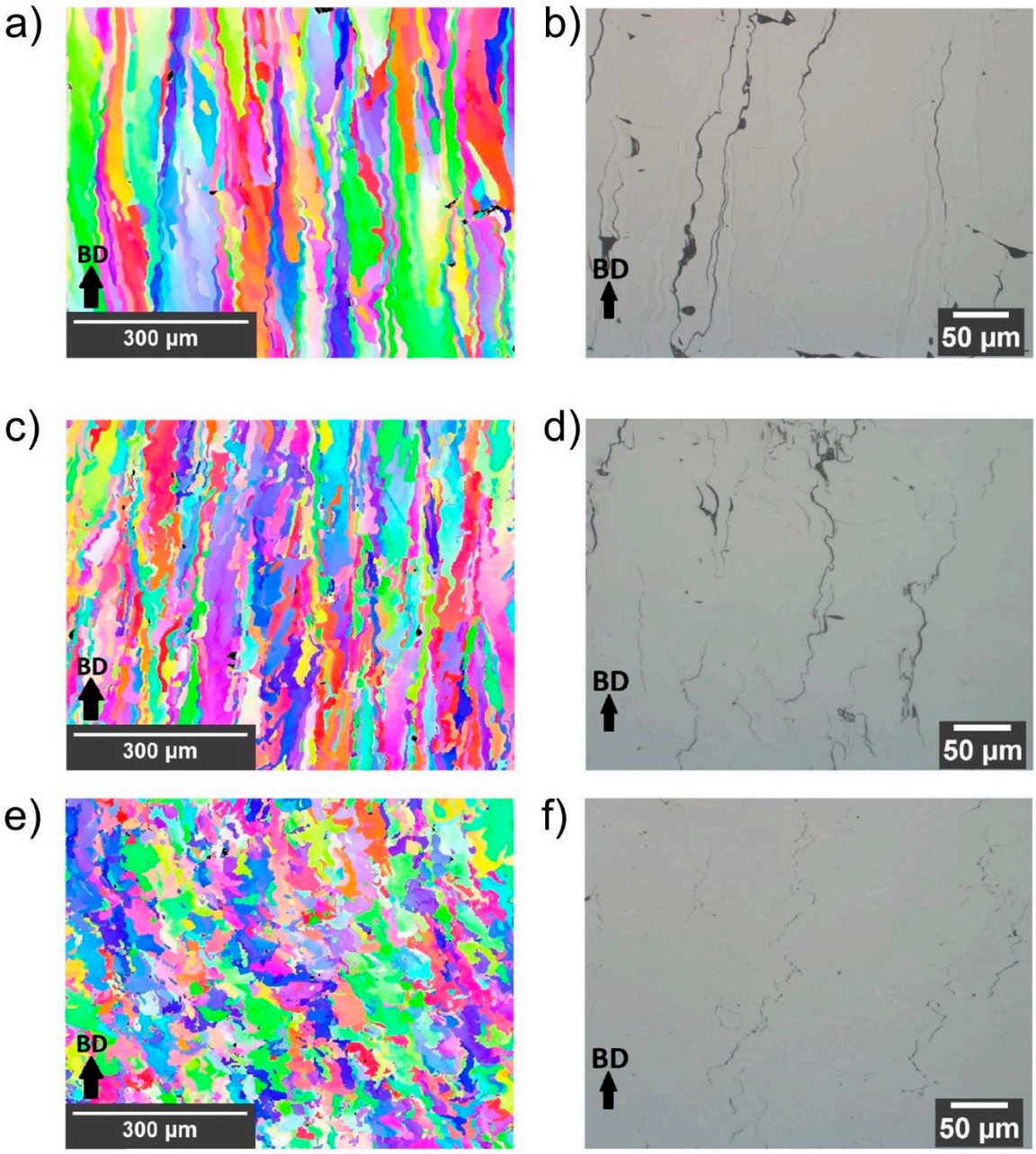

Figure 18. EBSD maps and optical microscopy images of W cubes made using SLM with different Re contents: (**a**,**b**) pure W cubes, (**c**,**d**) W with 5 wt.% Re cubes, and (**e**,**f**) W with 25 wt.% Re cubes. The laser power, hatch spacing, and scan speed were all kept constant at 200 W, 50 µm, and 400 mm/s, respectively. The build direction is also indicated in the image [127].

The inherent characteristics of alloying elements relieve stress by compensating for the shrinkage experienced as W solidifies (a direct consequence of its elevated melting point). This phenomenon plays a direct role in minimizing microcracking [110]. Further contributions from Cr result in grain refinement, indirectly aiding in crack mitigation. Cr induces a Cr-rich Cr-W phase to optimize grain refinement [86]. In conventional fabrication techniques of W-based alloys, adding Ti as an alloying element creates a heterogeneous chemical distribution, stalling the coarsening of nanostructured microstructures [152], whereas adding Ir strengthens grain boundary cohesion, optimizes dislocation mobility, and subsequently deters crack formation [153]. These alloying additions (Ti and Ir) may be beneficial in materials design for AM as well.

4.2.2. Ceramic Dispersions (W Composites)

Incorporating ceramic particles in W has been shown to enhance composite resistance to cracking. W's challenges with oxide retention and the power balling effect are clear indicators of oxidation difficulties, but solutions are on hand. The integration of La_2O_3 not only bolsters radiation resistance but also provides an indirect solution to the problem of interstitial contamination. Innovations like nanopore segregation have been introduced, inducing and identifying crack initiation. Achieving a high theoretical density range of 96–98.5%, combined with the optimal conditions characterized by elevated laser energy density and low oxygen levels, represent meaningful advancements in countering these challenges.

W-Y_2O_3 composites offer a refined grain size and commendable low-temperature ductility [42]. Based on EBSD grain size, and grain misorientation distribution studies of W-Y_2O_3 composites, the use of nano-sized Y_2O_3 particles leads to grain refinement and a greater occurrence of LAGBs. The concomitant reduction in HAGBs (which are more susceptible to cracking) markedly reduces cracking in the resulting W composites (Figure 19) [42]. Introducing micron-sized Y_2O_3 dispersions into W does not lead to grain refinement, although this increases the fraction of LAGBs (Figure 19c,d). However, when nano-sized Y_2O_3 dispersions are used in the composite, the fraction of LAGBs and grain size are both reduced (Figure 19e,f).

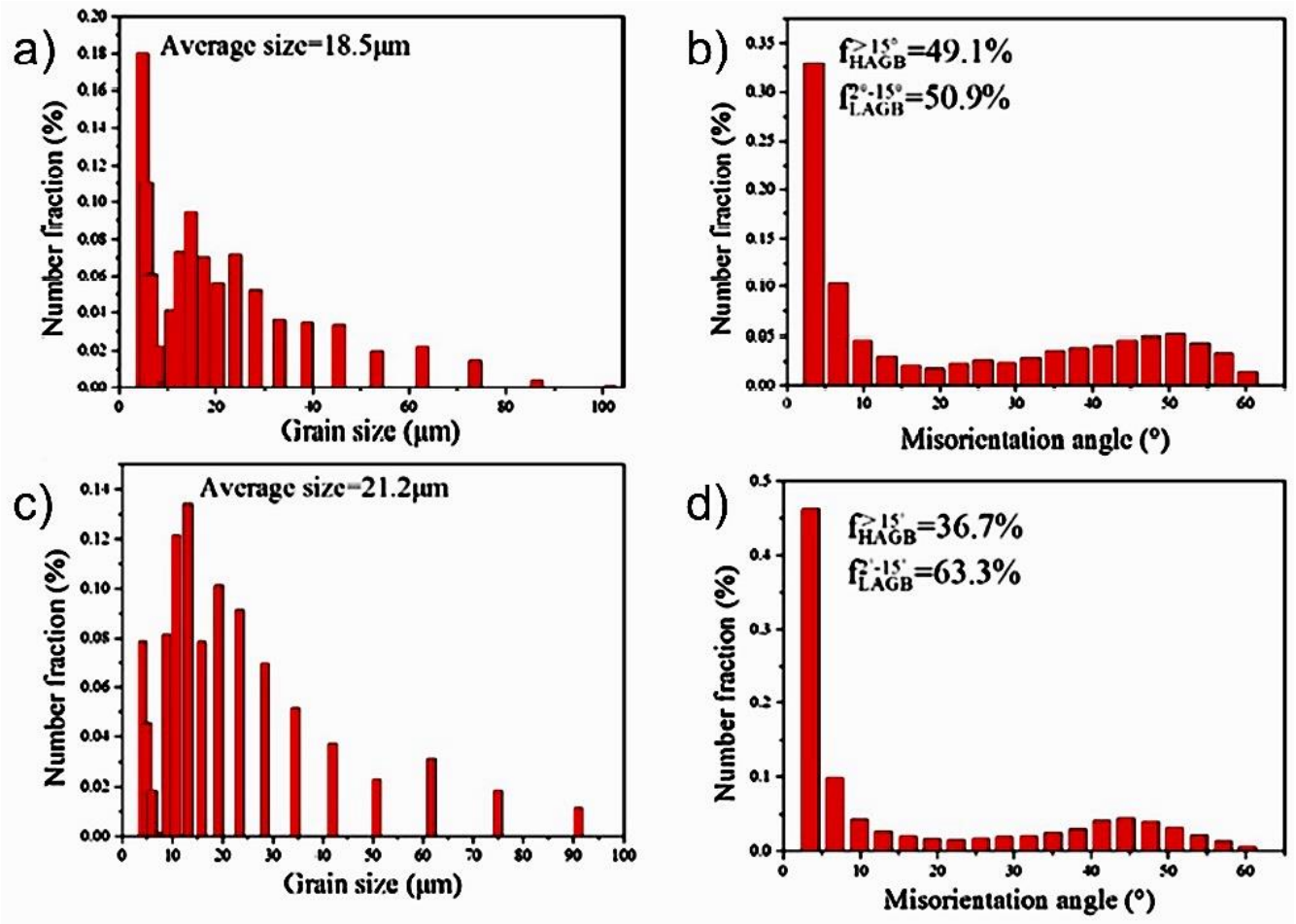

Figure 19. *Cont.*

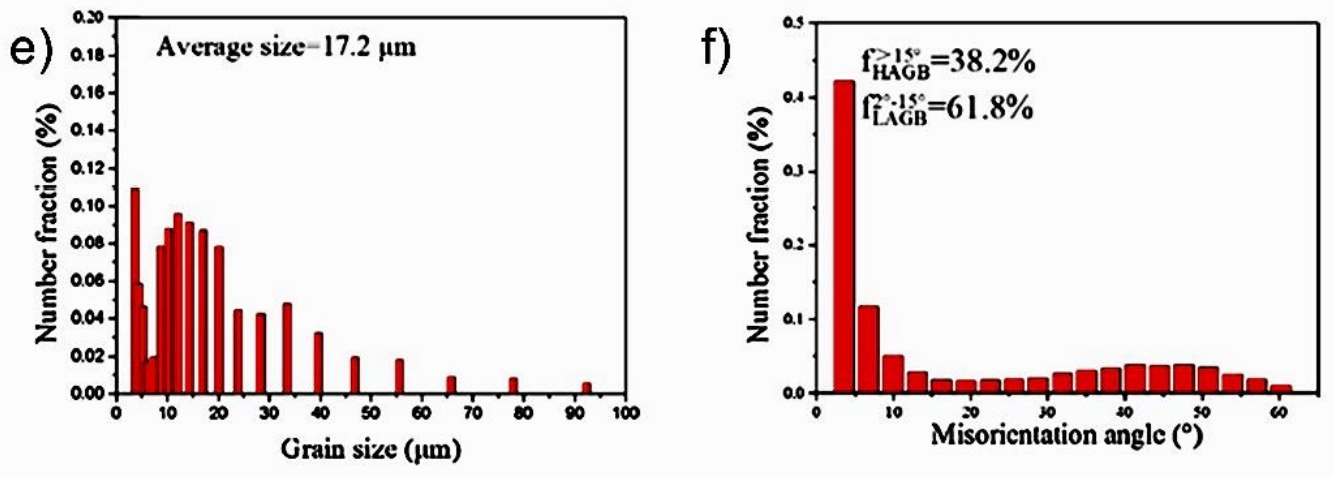

Figure 19. EBSD grain size distribution for SLM-fabricated samples: (**a**,**b**) pure W, (**c**,**d**) W-Y_2O_3 (micron-sized), and (**e**,**f**) W-Y_2O_3 (nano-sized) [42].

Li et al.'s study identified zirconium carbide (ZrC) as a crucial ceramic particle [120]. They showed that W-ZrC samples showed a remarkable reduction in crack density compared to pure W, showing fewer and more dispersed cracks in W-ZrC (Figure 20a,b). The images also reveal that, while pure W had long and densely distributed cracks, W-ZrC had shorter and sparser cracks (Figure 20c,d). This improved crack resistance is attributed to secondary-phase nanoparticles in W-ZrC, which refined the grain structure and captured oxygen impurities to hinder crack propagation. Achieving a fully uniform grain structure would require further efforts to ensure an even ZrC distribution. Li et al.'s study highlighted ZrC's role in reducing crack density, promoting finer grains, and extending grain boundaries. Their bright field TEM, HRTEM (high-resolution transmission electron microscopy), and high-angle annular dark field images (Figure 21a–c) along with EDS chemical maps (Figure 21d–h) at various magnifications, and the SAEDP (selected-area electron diffraction pattern) of selected nanoparticles (Figure 21f) provide compelling evidence of ZrC's capacity to capture and bind oxygen to form ZrO_y particles. This mechanism is a highly effective means of mitigating embrittlement [60,120].

Tantalum carbide (TaC) particles in W also play an important role in crack mitigation. This is achieved via the dual action of initiating in situ W_2C phase formations and promoting oxygen consumption through TaO_x formation, which collectively suppresses cracks [141,150]. Titanium carbide (TiC), while predominantly increasing hardness, may indirectly improve crack resistance due to the improved mechanical properties of the composite [42,47,141,150]. Hafnium carbide (HfC) dispersion in conventionally fabricated W alloys has provided excellent thermal stability and tensile properties of composites [154,155]. This can be a useful feature to have for materials design in the AM of W as well.

4.3. Alloying and Ceramic Dispersions for Mechanical Properties Adjustments

Besides mitigating the problems discussed above, alloying confers additional benefits. Fe integration in W alloys during AM strengthens the resulting material due to the formation of secondary or precipitated phases. This is due to the possible peritectic reaction between Fe and W during non-equilibrium solidification, leading to the emergence of intermetallic phases such as Fe_7W_6 and Fe_2W. This formation significantly increases the hardness of the W–Fe alloy [60,73,146]. Ni addition enhances the alloy's tensile strength and fracture toughness [74,130]. Nb provides solid solution strengthening and similarly improves the mechanical properties of the alloy [110]. The inclusion of Ta and other group V and IV transition metals improves the intrinsic ductility of W alloys. In particular, Ta not only enhances ductility but also increases the hardness of resultant alloys [141–144].

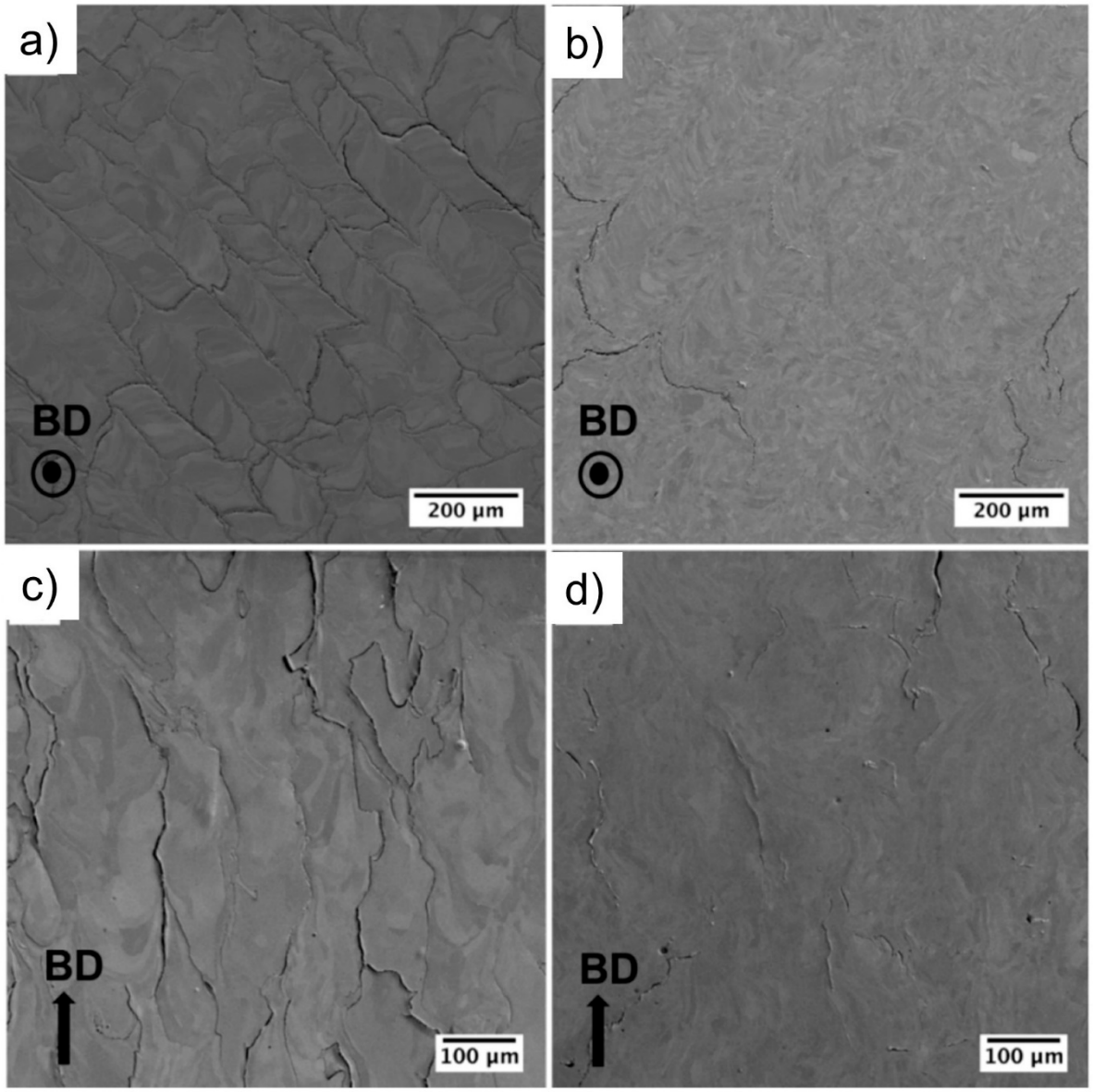

Figure 20. SEM images of SLM-fabricated pure W and W-ZrC nanocomposites: (**a**,**c**) the top and side surface of pure W cubes, and (**b**,**d**) the top and side surface of W-ZrC cubes. The build direction (BD) is also indicated in the image [120].

The incorporation of Ti, Ir, and Hf in conventionally fabricated W alloys achieves multiple objectives as they influence the mechanical properties in different ways. They increase recrystallization temperatures and, as potent carbide formers, mitigate the adverse effects of carbon impurities on the alloy's mechanics, elevate the recrystallization temperatures, and improve W's low-temperature ductility and high-temperature strength [152–156].

Since unalloyed W exhibits limited plasticity, studies have predominantly focused on reporting compression test results. Conversely, a wealth of tensile test results is available for W alloys processed using AM (Figure 22). Alloying elements play a pivotal role in enhancing the tensile properties of W, notably its elongation, which is otherwise limited or non-existent in unalloyed W. The strength and elongation of W alloys vary depending on compositions (Figure 22a,b). Wang et al. [74] reported a W–15% Ni alloy with a UTS of 560 MPa and 3.75% elongation, while W–7% Ni–3% Fe showed a UTS of 1037 MPa and 3.5% elongation [71], and W–4.6%Ni–2.4% Fe fabricated via powder extrusion 3D printing and sintering showed a UTS of 1040 MPa and remarkably high (20.7%) elongation

(Figure 22a,b) [133]. Ultrashort-time laser liquid phase sintering processing for W heavy alloy resulted in a UTS of 1374 MPa, and 8.5% elongation (Figure 22a,b) [85].

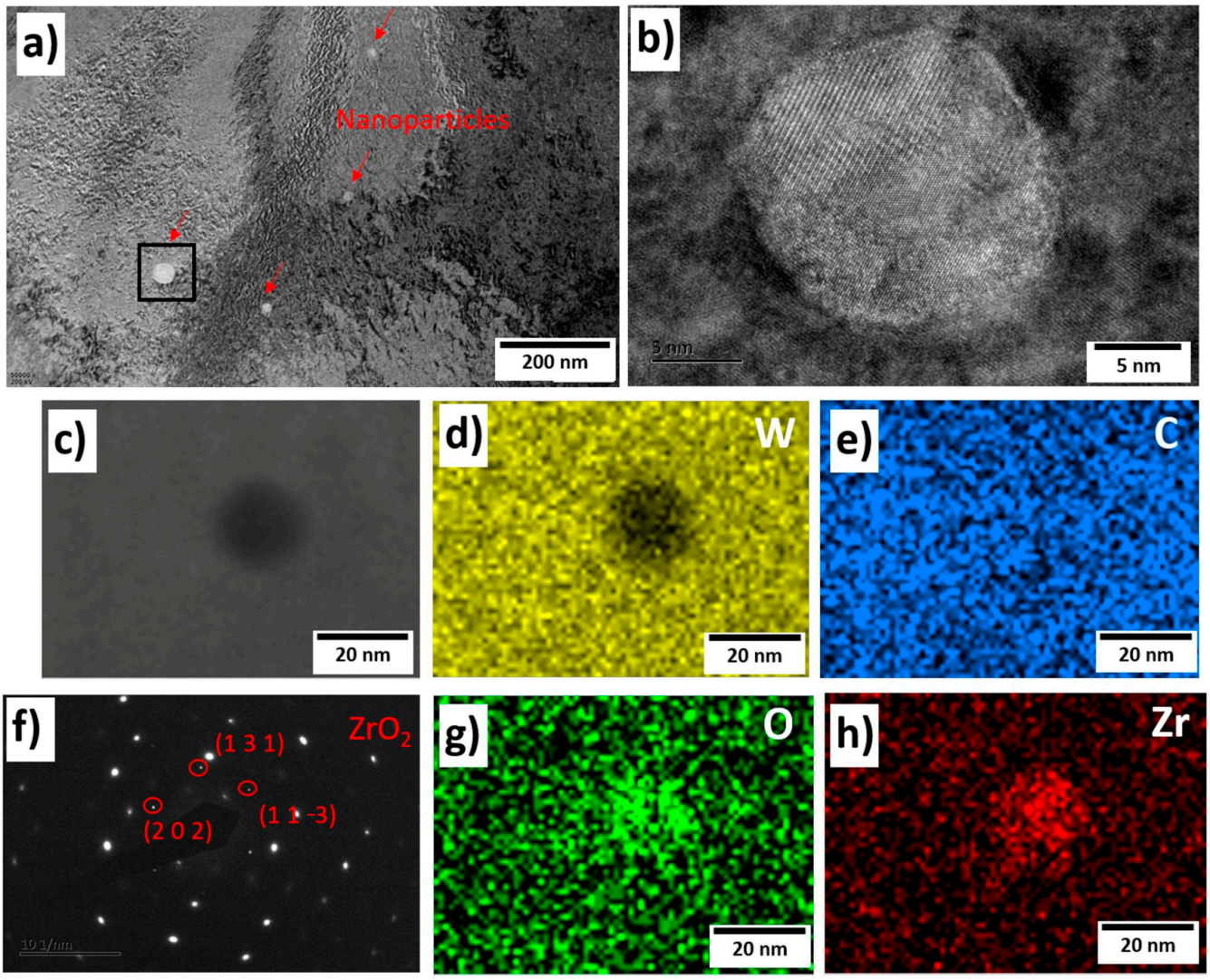

Figure 21. Analysis of the nanoparticle's dispersion in the SLM-fabricated W-ZrC nanocomposites: (**a**) distribution of nanoparticles, (**b**) the high-resolution transmission electron microscope of the selected nanoparticle, (**c**) the high-angle annular dark field image, (**d**–**h**) its EDS elemental maps, and (**f**) the selected-area electron diffraction pattern of the selected nanoparticle [120].

Figure 22c depicts the microhardness of AM-fabricated W-based materials. Li et al. [145] examined the variation in Vickers microhardness due to VED in the context of W-3%Ta alloy. Operating at a substrate preheating temperature of 150 °C and a 67° layer angle, they reported a range of microhardness values from 493.8 to 535.6 Hv. This range correlated with VED values spanning 192 to 1000 J/mm^3, with an average microhardness of 505.7 Hv. An upward trend in relative density was concurrently observed as VED values increased. Conversely, Bose et al. [86] reported the highest microhardness achievement of 966 Hv for a W-Cr component produced through binder jetting and sintering at 1500 °C for 1 h, demonstrating a striking contrast to the above trends. Zhang et al. [130] and Yan et al. [136] showed a contrasting narrative, showcasing a decline in hardness with an incremental influx of Ni in W-Ni and W-Ni-Cu systems. In a related study, Zhang et al. [130] highlighted a gradient of hardness reduction with the distance from the base of SLM-fabricated samples, plummeting from 810 to 300 Hv for W-10%Ni and from 490 to 250 Hv for W-40Ni.

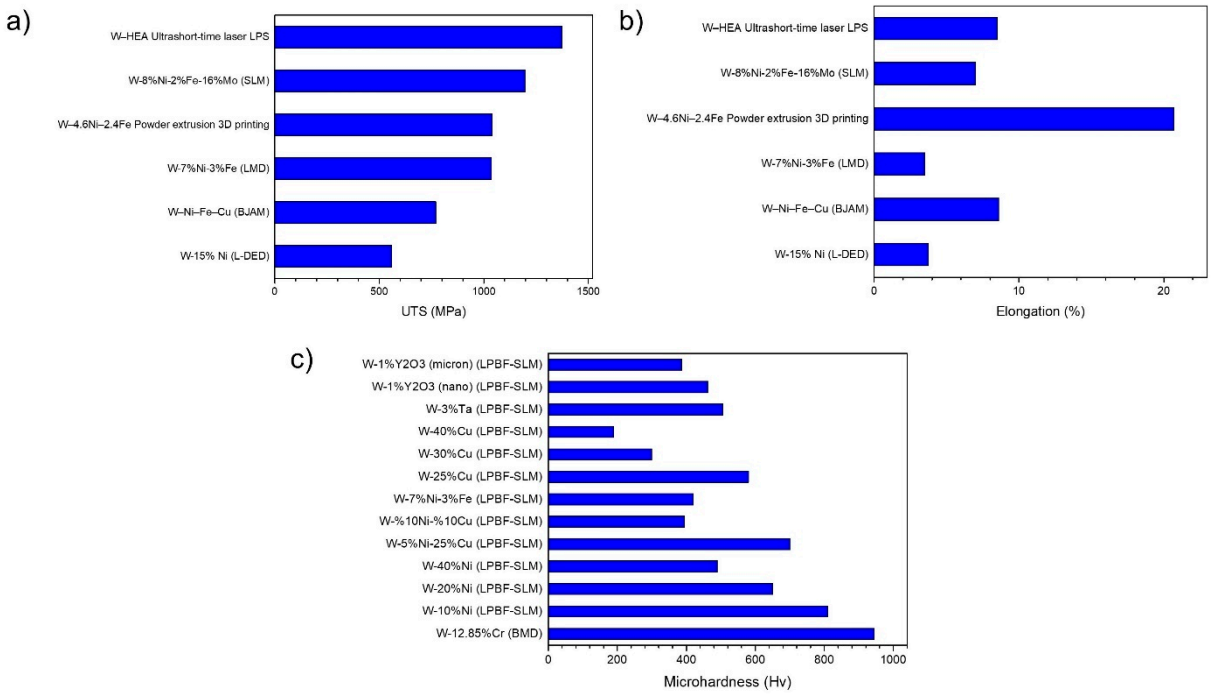

Figure 22. Mechanical properties of AM-fabricated W alloys: (**a**) ultimate tensile strength, (**b**) elongation, and (**c**) microhardness.

Ivekovic et al. [132] noted a decline in hardness post-heat treatment of SLM-fabricated W-7Ni-3Fe samples, which diverged from the augmentation in hardness expected. Conversely, Wang et al. [135] demonstrated that an escalation in the microhardness of W-Ni-Cu alloys, ranging from 360 to 395 Hv, was linked to increasing VED. This phenomenon is attributed to the formation of finer grain sizes owing to elevated melt pool temperatures. Moreover, Hu et al. [42] brought nano-structural considerations into the equation, underscoring the influence of grain size. They documented an upswing in hardness with the decreasing grain size of Y_2O_3 particles, transitioning from micro- to nano-scale dimensions.

These findings underscore the fact that enhanced and/or adjusted mechanical properties are achievable through alloying in the AM of W-based materials.

4.4. Alloying for Other Specific Purposes

The addition of Ta to W alloys is pivotal for reducing fuzz formation. Ta has demonstrated its capability to reduce fuzz during He plasma irradiation, making these alloys suitable for nuclear applications [140]. Furthermore, W alloys formulated with the Cr-Y combination exhibit self-passivation behavior in conventional fabrication. This intrinsic property makes W alloys integrated with Cr-Y especially useful in high-temperature applications [60,157].

Overall, the addition of alloying elements activates several mechanisms to enhance various properties (Table 8), which are as follows. Alloying elements such as Ta, Re, and Ni can act as grain refiners in W-based alloys. These elements reduce the grain size by inhibiting grain growth during solidification, resulting in a finer and more uniform microstructure [158]. Fine-grained microstructures typically exhibit higher strength and improved toughness due to the grain boundary strengthening mechanism. Alloying elements like Mo and Ti lead to solid solution strengthening [159]. These elements distort the W lattice and impede dislocation motion, thereby enhancing the yield strength and overall mechanical properties of the alloy. This mechanism is particularly beneficial in improving the high-temperature strength of W alloys. Certain alloying elements can form stable second phases or precipitates within the W matrix [160]. For example, carbide-forming elements such as carbon C can produce W carbides (WC) that enhance the hardness

and wear resistance of the alloy. These second phases also contribute to the overall strength by hindering dislocation movement. Alloying with elements such as Cr and Si can improve the oxidation resistance of W alloys [161]. These elements form protective oxide layers on the surface, which act as barriers to further oxidation, thereby enhancing the performance of W components in high-temperature environments [162]. Other elements like Re improve the ductility of W alloys by reducing the DBTT [128]. This brings about a more ductile fracture behavior and better toughness at lower temperatures, which is crucial for applications where mechanical shock or impact resistance is required.

5. Conclusions

Overall, the proposed solutions, which include optimizing process parameters, refining powder characteristics, implementing post-processing treatments, and employing alloying elements, are essential to address the fundamental issues of densification and mechanical properties in W-based materials. Here, we provide a detailed discussion of how each approach contributes to improving densification and mechanical properties, supported by the relevant literature.

1. Powder Characteristics

Particle Size and morphology: Utilizing W powder with a well-controlled particle size distribution and spherical morphology enhances flowability, packing density, and uniform layer formation during the built cycle. These characteristics are crucial for achieving high relative density and consistent microstructures, as evidenced by improved mechanical properties in various studies.

Powder purity: High-purity W powder minimizes contaminants that can cause defects and degrade mechanical properties. Ensuring powder purity is fundamental for producing high-quality components with superior mechanical integrity.

2. Process Parameter Optimization

Laser power and scan speed: By carefully adjusting the laser power and scan speed, we can ensure adequate energy input for the complete melting of tungsten powder while avoiding defects such as keyhole porosity and excessive vaporization. Optimal control of these parameters results in improved densification and reduced residual stresses. A maximum density of 99.2% in SLM and 100% in EBM was demonstrated by adjusting process parameters.

Volumetric energy density (VED): Our study emphasizes the critical role of VED in balancing energy input to promote full melting and minimize defects. Extremely high VED can introduce porosity and fusion issues, while insufficient VED can result in incomplete melting. Optimizing VED is essential for achieving high relative density and enhancing mechanical properties.

3. Thermal Management Strategies

Controlled atmosphere: Using an inert gas atmosphere of argon or nitrogen during the AM process prevents oxidation and contamination, preserving the material's purity and mechanical properties. While the majority of studies used argon, processing in a nitrogen atmosphere could enhance the microstructure and mechanical performance of tungsten parts.

Substate preheat: Utilizing a heated substrate plate in PBF processes is necessary to control cooling rates and mitigate thermal gradients such as built-up thermal residual stresses within the material, and improves material formation and properties. In most cases, the substrate is preheated in the range of 500 °C to 1000 °C in SLM and up to 1800 °C in EBM to eliminate crack formation.

Optimized scan strategies: Utilizing optimized scanning strategies such as alternating scan directions, island scanning, and contour scanning can distribute heat more evenly across the build area, reducing localized thermal stresses. These strategies help in achieving uniform thermal profiles and minimizing warping and distortion.

4. Alloying Strategies

The introduction of alloying elements: Adding alloying elements such as Re, Ta, and Hf can significantly enhance the mechanical properties and processability of W. Re, for instance, is known to improve ductility and reduce the DBTT, refine the grain structure, and improve the toughness of W alloys.

The introduction of ceramic particles: carbide formers (e.g., TiC, ZrC) can be introduced, which act as grain refiners and strengthen the W matrix through dispersion strengthening to improve the hardness and wear resistance of W components.

5. Post-Processing Treatments

Heat treatment: Post-process heat treatments are vital for relieving residual stresses, promoting grain growth, and enhancing mechanical properties. Techniques such as annealing reduce micro-cracks and improve ductility.

Hot isostatic pressing (HIP): HIP applies high pressure and temperature to further densify the components, close remaining pores, and refine the microstructure. This results in significantly improved mechanical strength and integrity.

6. Future Directions

Although W-AM holds great promise for producing high-performance parts, its widespread adoption has been hindered by problems associated with W's inherent material properties and printability challenges. Research efforts into the AM of W should be prioritized through the fine-tuning of process parameters, as well as microstructural and material design. We believe in the possibilities of bringing W-AM into a new era of precision, sustainability, and widespread applicability through advancements in atomic-level understanding, and thermodynamic modeling, as well as through harnessing the power of data analytics.

1. Atomic-Level Understanding: The Key to Tailored Properties
   Further studies are needed to understand W at the atomic level, focusing on the local atomic structure and short-range order chemistry. Improving our understanding of the inherent atomic arrangement in W from the microscopic perspective will enable us to unlock new possibilities for tailored material properties and optimized performance.
2. Thermodynamic Modeling: A Roadmap for Alloy Design
   Integrating the thermodynamic calculation of phase diagram modeling into alloy design will play a key role in predicting phase equilibria and allow researchers to design W alloys with better control over composition and phase transitions. This thermodynamic approach ensures a systematic exploration of the uncharted alloy space, allowing materials with tailored properties to be developed. This provides insights into process optimization through thermal gradients, melt pool dynamics, and solidification rates, which are essential for minimizing porosity and achieving uniform microstructures.
3. Composite Design: Improved Innovative Composite
   Researchers can seek to synergize W with other advanced ceramics, to create composites that exhibit superior mechanical, thermal, and chemical properties. This approach opens avenues for tailoring W composites for specific applications across diverse industries.
4. Harnessing the Power of Data Analytics: Machine Learning and in situ Monitoring
   Researchers can leverage machine learning and statistical techniques to identify patterns and correlations which can help in the optimization of processing parameters. Multiphysics and multi-scale computational modeling are essential for establishing process–structure–property relationships in metal AM [163]. This paves the way for the development of a digital twin for W-AM. Further studies can also develop and implement advanced in situ process monitoring techniques during AM. The data generated during the real-time monitoring of temperature, microstructure evolution, and defect formation will provide valuable insights, enabling adaptive control strategies to enhance the quality and repeatability of W components.

5. Sustainable Manufacturing: the Hidden Cost of the Oxidation of W
   The high oxygen affinity of W and its influence extends beyond AM-fabricated parts. The high temperatures and heating profiles employed during AM processes can lead to the inadvertent oxidation of adjacent powder beds. This oxidation significantly affects the reusability of W powder, potentially increasing waste and negating the environmental and cost benefits of AM. Future research efforts should prioritize mitigating this hidden cost by a comprehensive understanding of W oxidation to minimize the impact of oxidation and maximize powder reusability.

Author Contributions: Conceptualization, M.Z., Y.T. and C.M.; methodology, M.Z., M.S. and N.W.; validation, Y.X., M.Z. and L.T.; formal analysis, M.Z., C.M. and M.S.; resources, M.Z., N.W. and Y.X.; data curation, S.R., X.C. and L.T.; writing—original draft preparation, M.Z., M.S., Y.T., S.R. and C.M.; writing—review and editing, M.Z., M.S., X.C., N.W., Y.X., S.R. and K.X.K.; visualization, M.Z., M.S. and K.X.K.; supervision, M.Z., Y.T. and M.S.; project administration, M.Z., C.M. and Y.T.; funding acquisition, C.M. and M.Z. All authors have read and agreed to the published version of the manuscript.

Funding: This research was funded by Zhejiang Province grant number: 2023C01SA393195, and Wenzhou City grant number: ZG2023036.

Data Availability Statement: No further data are available. All the data pertaining to this work are already included in the article.

Acknowledgments: The authors from Wenzhou Hongfong Electrical Alloy Co Ltd and its subsidiary acknowledge these generous financial supports.

Conflicts of Interest: Authors Mehrdad Zarinejad, Chengfa Mu, Lintao Tian, and Xiaotong Chen were employed by the company Wenzhou Hongfeng Electrical Alloy Co., Ltd. Authors Nian Wang, and Yonglong Xu were employed by the company Wenzhou Hongfeng Alloy Co., Ltd. The remaining authors declare that the research was conducted in the absence of any commercial or financial relationships that could be construed as a potential conflict of interest.

Abbreviations

List of abbreviations used in the manuscript along with their full forms.

Abbreviation	Term
AM	Additive manufacturing
BMD	Bound metal deposition
DED	Direct energy deposition
DBTT	Ductile-to-brittle transition temperatures
EBM	Electron beam melting
HAGBs	High-angle grain boundaries
LED	Line (laser) energy density
LPS	Liquid phase sintering
LAGBs	Low-angle grain boundaries
PBF	Powder bed fusion
W	Tungsten
VED	Volumetric energy density

References

1. Rieth, M.; Dudarev, S.L.; de Vicente, S.M.G.; Aktaa, J.; Ahlgren, T.; Antusch, S.; Armstrong, D.E.J.; Balden, M.; Baluc, N.; Barthe, M.-F.; et al. Recent progress in research on tungsten materials for nuclear fusion applications in Europe. *J. Nucl. Mater.* **2013**, *432*, 482–500. [CrossRef]
2. Xie, J.; Lu, H.; Lu, J.; Song, X.; Wu, S.; Lei, J. Additive manufacturing of tungsten using directed energy deposition for potential nuclear fusion application. *Surf. Coat. Technol.* **2021**, *409*, 126884. [CrossRef]
3. Katoh, Y.; Snead, L.L.; Garrison, L.M.; Hu, X.; Koyanagi, T.; Parish, C.M.; Edmondson, P.D.; Fukuda, M.; Hwang, T.; Tanaka, T.; et al. Response of unalloyed tungsten to mixed spectrum neutrons. *J. Nucl. Mater.* **2019**, *520*, 193–207. [CrossRef]
4. Wang, G.; Qin, Y.; Yang, S. Influence of Ni additions on the microstructure and tensile property of W-Cu composites produced by direct energy deposition. *J. Alloys Compd.* **2022**, *899*, 163272. [CrossRef]

5. Engwall, A.M.; Shin, S.J.; Bae, J.; Wang, Y.M. Enhanced properties of tungsten films by high-power impulse magnetron sputtering. *Surf. Coat. Technol.* **2019**, *363*, 191–197. [CrossRef]
6. Su, S.; Lu, Y. Densified W Cu composite fabricated via laser additive manufacturing. *Int. J. Refract. Met. Hard Mater.* **2020**, *87*, 105122. [CrossRef]
7. Oponowicz, A.; Marciszko-Wiąckowska, M.; Baczmański, A.; Klaus, M.; Genzel, C.; Wroński, S.; Kollbek, K.; Wróbel, M. Gradient of Residual Stress and Lattice Parameter in Mechanically Polished Tungsten Measured Using Classical X-rays and Synchrotron Radiation. *Metall. Mater. Trans. A* **2020**, *51*, 5945–5957. [CrossRef]
8. Iveković, A.; Omidvari, N.; Vrancken, B.; Lietaert, K.; Thijs, L.; Vanmeensel, K.; Vleugels, J.; Kruth, J.-P. Selective laser melting of tungsten and tungsten alloys. *Int. J. Refract. Met. Hard Mater.* **2018**, *72*, 27–32. [CrossRef]
9. Jia, Y.; Chang, S.; Du, X.; Guo, S. Corrosion Performance of Commercial Alloys and Refractory Metals in Conditions for Electrorefining of Spent Nuclear Fuels. *Crystals* **2023**, *13*, 817. [CrossRef]
10. Wei, Q.; Ramesh, K.T.; Schuster, B.E.; Kecskes, L.J.; Dowding, R.J. Nanoengineering opens a new era for tungsten as well. *JOM* **2006**, *58*, 40–44. [CrossRef]
11. Zinkle, S.J.; Ott, L.J.; Ingersoll, D.T.; Ellis, R.J.; Grossbeck, M.L. Overview of materials technologies for space nuclear power and propulsion. *AIP Conf. Proc.* **2002**, *608*, 1063–1073. [CrossRef]
12. Mani, M.; Madan, J.; Lee, J.H.; Lyons, K.W.; Gupta, S.K. Sustainability characterisation for manufacturing processes. *Int. J. Prod. Res.* **2014**, *52*, 5895–5912. [CrossRef]
13. Valivullah, L.; Mani, M.; Lyons, K.W.; Gupta, S.K. Manufacturing Process Information Models for Sustainable Manufacturing. In *Volume 1: Materials; Micro and Nano Technologies; Properties, Applications and Systems; Sustainable Manufacturing*; American Society of Mechanical Engineers: New York, NY, USA, 2014. [CrossRef]
14. Mani, M.; Lyons, K.W.; Gupta, S.K. Sustainability Characterization for Additive Manufacturing. *J. Res. Natl. Inst. Stand. Technol.* **2014**, *119*, 419. [CrossRef] [PubMed]
15. Moghimian, P.; Poirié, T.; Habibnejad-Korayem, M.; Zavala, J.A.; Kroeger, J.; Marion, F.; Larouche, F. Metal powders in additive manufacturing: A review on reusability and recyclability of common titanium, nickel and aluminum alloys. *Addit. Manuf.* **2021**, *43*, 102017. [CrossRef]
16. Mireles, O.; Rodriguez, O.; Gao, Y.; Philips, N. Additive Manufacture of Refractory Alloy C103 for Propulsion Applications. In *AIAA Propulsion and Energy 2020 Forum*; American Institute of Aeronautics and Astronautics: Reston, VA, USA, 2020. [CrossRef]
17. Ren, X.; Liu, H.; Lu, F.; Huang, L.; Yi, X. Effects of processing parameters on the densification, microstructure and mechanical properties of pure tungsten fabricated by optimized selective laser melting: From single and multiple scan tracks to bulk parts. *Int. J. Refract. Met. Hard Mater.* **2021**, *96*, 105490. [CrossRef]
18. Bai, S.; Liu, J.; Yang, P.; Huang, H.; Yang, L.-M. Femtosecond Fiber Laser Additive Manufacturing of Tungsten. In Proceedings of the SPIE 9738-24, San Francisco, CA, USA, 13–18 February 2016; Gu, B., Helvajian, H., Piqué, A., Eds.; SPIE: San Francisco, CA, USA, 2016. [CrossRef]
19. Müller, A.V.; Schlick, G.; Neu, R.; Anstätt, C.; Klimkait, T.; Lee, J.; Pascher, B.; Schmitt, M.; Seidel, C. Additive manufacturing of pure tungsten by means of selective laser beam melting with substrate preheating temperatures up to 1000 °C. *Nucl. Mater. Energy* **2019**, *19*, 184–188. [CrossRef]
20. Feng, F.; Lian, Y.; Wang, J.; Song, J.; Yan, B.; Liu, X. Mechanical Properties and Thermal Shock Performance of High-Energy-Rate-Forged W-1%TaC Alloy. *Crystals* **2022**, *12*, 1047. [CrossRef]
21. Wang, D.-Z.; Li, K.-L.; Yu, C.-F.; Ma, J.; Liu, W.; Shen, Z.-J. Cracking Behavior in Additively Manufactured Pure Tungsten. *Acta Metall. Sin. (Engl. Lett.)* **2019**, *32*, 127–135. [CrossRef]
22. Lassner, E.; Schubert, W.-D. *Tungsten*; Springer US: Boston, MA, USA, 1999. [CrossRef]
23. Mitteau, R.; Missiaen, J.M.; Brustolin, P.; Ozer, O.; Durocher, A.; Ruset, C.; Lungu, C.P.; Courtois, X.; Dominicy, C.; Maier, H.; et al. Recent developments toward the use of tungsten as armour material in plasma facing components. *Fusion. Eng. Des.* **2007**, *82*, 1700–1705. [CrossRef]
24. Vrancken, B.; Ganeriwala, R.K.; Matthews, M.J. Analysis of laser-induced microcracking in tungsten under additive manufacturing conditions: Experiment and simulation. *Acta Mater.* **2020**, *194*, 464–472. [CrossRef]
25. Elsayed, A.H.; Sayed, M.A.; Dawood, O.M.; Daoush, W.M. Effect of Transition Metals Oxides on the Physical and Mechanical Properties of Sintered Tungsten Heavy Alloys. *Crystals* **2020**, *10*, 825. [CrossRef]
26. Wang, L.; Wu, J.; Zhang, D. Properties evolution of additive manufacture used tungsten powders prepared by radio frequency induction plasma. *Int. J. Refract. Met. Hard Mater.* **2017**, *67*, 90–97. [CrossRef]
27. Zi, X.; Chen, C.; Wang, X.; Wang, P.; Zhang, X.; Zhou, K. Spheroidisation of tungsten powder by radio frequency plasma for selective laser melting. *Mater. Sci. Technol.* **2018**, *34*, 735–742. [CrossRef]
28. Gu, D.D.; Meiners, W.; Wissenbach, K.; Poprawe, R. Laser additive manufacturing of metallic components: Materials, processes and mechanisms. *Int. Mater. Rev.* **2012**, *57*, 133–164. [CrossRef]
29. Guo, M.; Gu, D.; Xi, L.; Du, L.; Zhang, H.; Zhang, J. Formation of scanning tracks during Selective Laser Melting (SLM) of pure tungsten powder: Morphology, geometric features and forming mechanisms. *Int. J. Refract Metals Hard Mater.* **2019**, *79*, 37–46. [CrossRef]
30. Wen, S.; Wang, C.; Zhou, Y.; Duan, L.; Wei, Q.; Yang, S.; Shi, Y. High-density tungsten fabricated by selective laser melting: Densification, microstructure, mechanical and thermal performance. *Opt. Laser Technol.* **2019**, *116*, 128–138. [CrossRef]

31. Gokcekaya, O.; Ishimoto, T.; Todo, T.; Wang, P.; Nakano, T. Influence of powder characteristics on densification via crystallographic texture formation: Pure tungsten prepared by laser powder bed fusion. *Addit. Manuf. Lett.* **2021**, *1*, 100016. [CrossRef]
32. Yang, G.; Yang, P.; Yang, K.; Liu, N.; Jia, L.; Wang, J.; Tang, H. Effect of processing parameters on the density, microstructure and strength of pure tungsten fabricated by selective electron beam melting. *Int. J. Refract. Metals Hard Mater.* **2019**, *84*, 105040. [CrossRef]
33. Gokuldoss, P.K.; Kolla, S.; Eckert, J.; Processes, A.M. Electron Beam Melting and Binder Jetting—Selection Guidelines. *Materials* **2017**, *10*, 672. [CrossRef] [PubMed]
34. Klahn, C.; Leutenecker, B.; Meboldt, M. Design Strategies for the Process of Additive Manufacturing. *Procedia CIRP* **2015**, *36*, 230–235. [CrossRef]
35. Vrancken, B.; King, W.E.; Matthews, M.J. In-situ characterization of tungsten microcracking in Selective Laser Melting. *Procedia CIRP* **2018**, *74*, 107–110. [CrossRef]
36. Sidambe, A.T.; Tian, Y.; Prangnell, P.B.; Fox, P. Effect of processing parameters on the densification, microstructure and crystallographic texture during the laser powder bed fusion of pure tungsten. *Int. J. Refract. Metals Hard Mater.* **2019**, *78*, 254–263. [CrossRef]
37. Rebesan, P.; Bonesso, M.; Gennari, C.; Dima, R.; Pepato, A.; Vedani, M. Tungsten Fabricated by Laser Powder Bed Fusion. *BHM Berg-Und Hüttenmännische Monatshefte* **2021**, *166*, 263–269. [CrossRef]
38. Tan, C.; Zhou, K.; Ma, W.; Attard, B.; Zhang, P.; Kuang, T. Selective laser melting of high-performance pure tungsten: Parameter design, densification behavior and mechanical properties. *Sci. Technol. Adv. Mater.* **2018**, *19*, 370–380. [CrossRef] [PubMed]
39. Chen, J.; Li, K.; Wang, Y.; Xing, L.; Yu, C.; Liu, H.; Ma, J.; Liu, W.; Shen, Z. The effect of hot isostatic pressing on thermal conductivity of additively manufactured pure tungsten. *Int. J. Refract. Met. Hard Mater.* **2020**, *87*, 105135. [CrossRef]
40. Field, A.C.; Carter, L.N.; Adkins, N.J.E.; Attallah, M.M.; Gorley, M.J.; Strangwood, M. The Effect of Powder Characteristics on Build Quality of High-Purity Tungsten Produced via Laser Powder Bed Fusion (LPBF). *Metall. Mater. Trans. A* **2020**, *51*, 1367–1378. [CrossRef]
41. Guo, M.; Gu, D.; Xi, L.; Zhang, H.; Zhang, J.; Yang, J.; Wang, R. Selective laser melting additive manufacturing of pure tungsten: Role of volumetric energy density on densification, microstructure and mechanical properties. *Int. J. Refract. Metals Hard Mater.* **2019**, *84*, 105025. [CrossRef]
42. Hu, Z.; Zhao, Y.; Guan, K.; Wang, Z.; Ma, Z. Pure tungsten and oxide dispersion strengthened tungsten manufactured by selective laser melting: Microstructure and cracking mechanism. *Addit. Manuf.* **2020**, *36*, 101579. [CrossRef]
43. Wang, D.; Yu, C.; Zhou, X.; Ma, J.; Liu, W.; Shen, Z. Dense Pure Tungsten Fabricated by Selective Laser Melting. *Appl. Sci.* **2017**, *7*, 430. [CrossRef]
44. Vrancken, B.; Ganeriwala, R.K.; Martin, A.A.; Matthews, M.J. Microcrack mitigation during laser scanning of tungsten via preheating and alloying strategies. *Addit. Manuf.* **2021**, *46*, 102158. [CrossRef]
45. Xiong, Z.; Zhang, P.; Tan, C.; Dong, D.; Ma, W.; Yu, K. Selective Laser Melting and Remelting of Pure Tungsten. *Adv. Eng. Mater.* **2020**, 22. [CrossRef]
46. Zhou, X.; Liu, X.; Zhang, D.; Shen, Z.; Liu, W. Balling phenomena in selective laser melted tungsten. *J. Mater. Process Technol.* **2015**, *222*, 33–42. [CrossRef]
47. Wu, Y. Manufacturing of tungsten and tungsten composites for fusion application via different routes. *Tungsten* **2019**, *1*, 80–90. [CrossRef]
48. Wang, D.; Wang, Z.; Li, K.; Ma, J.; Liu, W.; Shen, Z. Cracking in laser additively manufactured W: Initiation mechanism and a suppression approach by alloying. *Mater. Des.* **2019**, *162*, 384–393. [CrossRef]
49. Braun, J.; Kaserer, L.; Stajkovic, J.; Leitz, K.-H.; Tabernig, B.; Singer, P.; Leibenguth, P.; Gspan, C.; Kestler, H.; Leichtfried, G. Molybdenum and tungsten manufactured by selective laser melting: Analysis of defect structure and solidification mechanisms. *Int. J. Refract. Met. Hard Mater.* **2019**, *84*, 104999. [CrossRef]
50. Yamamoto, T.; Hara, M.; Hatano, Y. Effects of fabrication conditions on the microstructure, pore characteristics and gas retention of pure tungsten prepared by laser powder bed fusion. *Int. J. Refract. Metals Hard Mater.* **2021**, *95*, 105410. [CrossRef]
51. Enneti, R.K.; Morgan, R.; Atre, S.V. Effect of process parameters on the Selective Laser Melting (SLM) of tungsten. *Int. J. Refract. Met. Hard Mater.* **2018**, *71*, 315–319. [CrossRef]
52. Zhang, D.; Cai, Q.; Liu, J. Formation of Nanocrystalline Tungsten by Selective Laser Melting of Tungsten Powder. *Mater. Manuf. Process.* **2012**, *27*, 1267–1270. [CrossRef]
53. Zhang, J.; Gu, D.; Yang, Y.; Zhang, H.; Chen, H.; Dai, D.; Lin, K. Influence of Particle Size on Laser Absorption and Scanning Track Formation Mechanisms of Pure Tungsten Powder During Selective Laser Melting. *Engineering* **2019**, *5*, 736–745. [CrossRef]
54. Deprez, K.; Vandenberghe, S.; Van Audenhaege, K.; Van Vaerenbergh, J.; Van Holen, R. Rapid additive manufacturing of MR compatible multipinhole collimators with selective laser melting of tungsten powder. *Med. Phys.* **2013**, *40*, 012501. [CrossRef]
55. Sidambe, A.T.; Judson, D.S.; Colosimo, S.J.; Fox, P. Laser powder bed fusion of a pure tungsten ultra-fine single pinhole collimator for use in gamma ray detector characterisation. *Int. J. Refract. Met. Hard Mater.* **2019**, *84*, 104998. [CrossRef]
56. Gear, J.I.; Taprogge, J.; White, O.; Flux, G.D. Characterisation of the attenuation properties of 3D-printed tungsten for use in gamma camera collimation. *EJNMMI Phys.* **2019**, *6*, 1. [CrossRef] [PubMed]
57. Zhou, K.; Chen, W.; Yang, Y.; Li, R.; Dong, L.; Fu, Y.-Q. Microstructure and mechanical behavior of porous tungsten skeletons synthesized by selected laser melting. *Int. J. Refract. Met. Hard Mater.* **2022**, *103*, 105769. [CrossRef]

58. Morcos, P.; Elwany, A.; Karaman, I.; Arróyave, R. Review: Additive manufacturing of pure tungsten and tungsten-based alloys. *J. Mater. Sci.* **2022**, *57*, 9769–9806. [CrossRef]
59. Omole, S.; Lunt, A.; Kirk, S.; Shokrani, A. Advanced Processing and Machining of Tungsten and Its Alloys. *J. Manuf. Mater. Process.* **2022**, *6*, 15. [CrossRef]
60. Pan, S.-H.; Yao, G.-C.; Cui, Y.-N.; Meng, F.-S.; Luo, C.; Zheng, T.-Q.; Singh, G. Additive manufacturing of tungsten, tungsten-based alloys, and tungsten matrix composites. *Tungsten* **2023**, *5*, 1–31. [CrossRef]
61. Talignani, A.; Seede, R.; Whitt, A.; Zheng, S.; Ye, J.; Karaman, I.; Kirka, M.M.; Katoh, Y.; Wang, Y.M. A review on additive manufacturing of refractory tungsten and tungsten alloys. *Addit. Manuf.* **2022**, *58*, 103009. [CrossRef]
62. Galati, M. Electron beam melting process. In *Additive Manufacturing*; Elsevier: Amsterdam, The Netherlands, 2021; pp. 277–301. [CrossRef]
63. Ellis, E.A.I.; Sprayberry, M.A.; Ledford, C.; Hankwitz, J.P.; Kirka, M.M.; Rock, C.D.; Horn, T.J.; Katoh, Y.; Dehoff, R.R. Processing of tungsten through electron beam melting. *J. Nucl. Mater.* **2021**, *555*, 153041. [CrossRef]
64. Zhang, H.; Carriere, P.R.; Amoako, E.D.; Rock, C.D.; Thielk, S.U.; Fletcher, C.G.; Horn, T.J. Microstructure and Elevated Temperature Flexure Testing of Tungsten Produced by Electron Beam Additive Manufacturing. *JOM* **2023**, *75*, 4094–4107. [CrossRef]
65. Dorow-Gerspach, D.; Kirchner, A.; Loewenhoff, T.; Pintsuk, G.; Weißgärber, T.; Wirtz, M. Additive manufacturing of high density pure tungsten by electron beam melting. *Nucl. Mater. Energy* **2021**, *28*, 101046. [CrossRef]
66. Wang, J.; Yao, D.; Li, M.; An, X.; Li, S.; Hou, W.; Zhang, X.; Yang, G.; Wang, J.; Wang, L. Hierarchical effects of multi-layer powder spreading in the electron beam powder bed fusion additive manufacturing of pure tungsten material. *Addit. Manuf.* **2022**, *55*, 102835. [CrossRef]
67. Zhao, X.; An, N.; Yang, G.; Wang, J.; Tang, H.; Li, M.; Zhou, J. Enhancing standard finite element codes with POD for reduced order thermal analysis: Application to electron beam melting of pure tungsten. *Mater. Today Commun.* **2021**, *29*, 102796. [CrossRef]
68. Fernandez-Zelaia, P.; Kirka, M.; Campbell, Q.; Rojas, J.O.; Rossy, A.M.; Ledford, C. Electron Beam Powder Bed Fusion Additive Manufacturing of Refractory Metals. In *Proceedings of the Powdermet/Tungsten 2021*; Orlando, FL, USA, 20–23 June 2021. Available online: https://www.osti.gov/biblio/1832704 (accessed on 15 July 2024).
69. Liao, W.-B.; Liu, Z.-Y.; He, M.-J.; Feng, C.; Wang, F.; Huang, J. Effect of Electron Beam Remelting Treatments on the Microstructure and Properties of Atmospheric Plasma Sprayed Tungsten Coatings. *J. Therm. Spray. Technol.* **2021**, *30*, 2128–2137. [CrossRef]
70. Jeong, W.; Kwon, Y.-S.; Kim, D. Three-dimensional printing of tungsten structures by directed energy deposition. *Mater. Manuf. Process.* **2019**, *34*, 986–992. [CrossRef]
71. Wang, Y.P.; Ma, S.Y.; Yang, X.S.; Zhou, Y.Z.; Liu, X.; Li, J.F.; Zhang, J.J.; Li, C.; Wang, X.Y.; Le, G.M.; et al. Microstructure and strengthening mechanisms of 90W–7Ni–3Fe alloys prepared using laser melting deposition. *J. Alloys Compd.* **2020**, *838*, 155545. [CrossRef]
72. Wang, G.-Y.; Gu, S.-N.; Yang, S. Microstructure and properties of tungsten heavy alloys fabricated by laser direct deposition. *Mater. Sci. Technol.* **2017**, *33*, 415–420. [CrossRef]
73. Li, C.; Ma, S.; Liu, X.; Li, J.; Le, G. Microstructures and properties of 80W-20Fe alloys prepared using laser melting deposition process. *Int. J. Refract. Met. Hard Mater.* **2018**, *77*, 113–119. [CrossRef]
74. Wang, G.; Sun, X.; Huang, M.; Qin, Y.; Yao, Y.; Yang, S. Influence of processing parameters on the microstructure and tensile property of 85 W-15Ni produced by laser direct deposition. *Int. J. Refract. Met. Hard Mater.* **2019**, *82*, 227–233. [CrossRef]
75. Zhou, S.; Wang, L.; Liang, Y.-J.; Zhu, Y.; Jian, R.; Wang, B.; Wang, L.; Xue, Y.; Wang, F.; Cai, H.; et al. A strategy to achieve high-strength WNiFe composite-like alloys with low W content by laser melting deposition. *Mater. Des.* **2020**, *190*, 108554. [CrossRef]
76. DebRoy, T.; Wei, H.L.; Zuback, J.S.; Mukherjee, T.; Elmer, J.W.; Milewski, J.O.; Beese, A.M.; Wilson-Heid, A.; De, A.; Zhang, W. Additive manufacturing of metallic components—Process, structure and properties. *Prog. Mater. Sci.* **2018**, *92*, 112–224. [CrossRef]
77. Li, C.; Wang, Y.; Ma, S.; Yang, X.; Li, J.; Zhou, Y.; Liu, X.; Tang, J.; Wang, X.; Le, G. Densification, microstructural evolutions of 90W-7Ni-3Fe tungsten heavy alloys during laser melting deposition process. *Int. J. Refract. Met. Hard Mater.* **2020**, *91*, 105254. [CrossRef]
78. Marinelli, G.; Martina, F.; Lewtas, H.; Hancock, D.; Mehraban, S.; Lavery, N.; Ganguly, S.; Williams, S. Microstructure and thermal properties of unalloyed tungsten deposited by Wire + Arc Additive Manufacture. *J. Nucl. Mater.* **2019**, *522*, 45–53. [CrossRef]
79. Pixner, F.; Buzolin, R.; Warchomicka, F.; Pilz, A.; Enzinger, N. Wire-based electron beam additive manufacturing of tungsten. *Int. J. Refract. Met. Hard Mater.* **2022**, *108*, 105917. [CrossRef]
80. Stawovy, M.T.; Myers, K.; Ohm, S. Binder jet printing of tungsten heavy alloy. *Int. J. Refract. Met. Hard Mater.* **2019**, *83*, 104981. [CrossRef]
81. Doddapaneni, V.V.K.; Lee, K.; Aysal, H.E.; Paul, B.K.; Pasebani, S.; Sierros, K.A.; Okwudire, C.E.; Chang, C. A Review on Progress, Challenges, and Prospects of Material Jetting of Copper and Tungsten. *Nanomaterials* **2023**, *13*, 2303. [CrossRef]
82. Ottensmeyer, M.; Sabet, H.; Furenlid, L.; May, M.; Kupinski, M. Collimator fabrication techniques: A comparative study. *J. Nucl. Med.* **2023**, *64*, P1600. Available online: http://jnm.snmjournals.org/content/64/supplement_1/P1600.abstract (accessed on 15 July 2024).
83. Bose, A.; Reidy, J.P.; Tuncer, N.; Jorgensen, L. Processing of tungsten heavy alloy by extrusion-based additive manufacturing. *Int. J. Refract. Met. Hard Mater.* **2023**, *110*, 106021. [CrossRef]

84. Huang, N.; Cook, O.J.; Argüelles, A.P.; Beese, A.M. Review of Process–Structure–Property Relationships in Metals Fabricated Using Binder Jet Additive Manufacturing. *Metallogr. Microstruct. Anal.* **2023**, *12*, 883–905. [CrossRef]
85. Zhou, S.; Liang, Y.-J.; Zhu, Y.; Wang, B.; Wang, L.; Xue, Y. Ultrashort-time liquid phase sintering of high-performance fine-grain tungsten heavy alloys by laser additive manufacturing. *J. Mater. Sci. Technol.* **2021**, *90*, 30–36. [CrossRef]
86. Bose, A.; Schuh, C.A.; Tobia, J.C.; Tuncer, N.; Mykulowycz, N.M.; Preston, A.; Barbati, A.C.; Kernan, B.; Gibson, M.A.; Krause, D.; et al. Traditional and additive manufacturing of a new Tungsten heavy alloy alternative. *Int. J. Refract. Met. Hard Mater.* **2018**, *73*, 22–28. [CrossRef]
87. Du, Z.-Y.; Lv, Y.-Q.; Han, Y.; Fan, J.-L.; Ye, L. Sintering densification behavior and kinetic mechanism of nano-tungsten powder prepared by sol-spray drying. *Tungsten* **2020**, *2*, 371–380. [CrossRef]
88. Han, Y.; Fan, J.; Liu, T.; Cheng, H.; Tian, J. The effect of trace nickel additive and ball milling treatment on the near-full densification behavior of ultrafine tungsten powder. *Int. J. Refract. Met. Hard Mater.* **2012**, *34*, 18–26. [CrossRef]
89. Thompson, S.M.; Bian, L.; Shamsaei, N.; Yadollahi, A. An overview of Direct Laser Deposition for additive manufacturing; Part I: Transport phenomena, modeling and diagnostics. *Addit. Manuf.* **2015**, *8*, 36–62. [CrossRef]
90. Karafi, T.; Tahiri, A.; Chabba, H.; Idiri, M.; Boubeker, B. Effect of Grain-Size in Nanocrystalline Tungsten on Hardness and Dislocation Density: A Molecular Dynamics Study. *Crystals* **2023**, *13*, 469. [CrossRef]
91. Kozyrev, N.V.; Gordeev, V.V. Thermodynamic Properties and Equation of State for Tungsten. *Crystals* **2023**, *13*, 1470. [CrossRef]
92. Griffiths, V.; Scanlan, J.P.; Eres, M.H.; Martinez-Sykora, A.; Chinchapatnam, P. Cost-driven build orientation and bin packing of parts in Selective Laser Melting (SLM). *Eur. J. Oper. Res.* **2019**, *273*, 334–352. [CrossRef]
93. Ren, K.; Di, Y.; Wang, G.; Wang, L.; Wang, H.; Rong, Y. Forward calculation model for utilization of energy and mass in laser-directed energy deposition. *Addit. Manuf.* **2023**, *68*, 103512. [CrossRef]
94. Mohammadhosseini, A.; Masood, S.H.; Fraser, D.; Jahedi, M. Dynamic compressive behaviour of Ti-6Al-4V alloy processed by electron beam melting under high strain rate loading. *Adv. Manuf.* **2015**, *3*, 232–243. [CrossRef]
95. Yang, S.F.; Li, C.W.; Chen, A.Y.; Gan, B.; Gu, J.F. Microstructure and corrosion resistance of stainless steel manufactured by laser melting deposition. *J. Manuf. Process* **2021**, *65*, 418–427. [CrossRef]
96. Ziaee, M.; Crane, N.B. Binder jetting: A review of process, materials, and methods. *Addit. Manuf.* **2019**, *28*, 781–801. [CrossRef]
97. Wei, C.; Liu, L.; Gu, Y.; Huang, Y.; Chen, Q.; Li, Z.; Li, L. Multi-material additive-manufacturing of tungsten-copper alloy bimetallic structure with a stainless-steel interlayer and associated bonding mechanisms. *Addit. Manuf.* **2022**, *50*, 102574. [CrossRef]
98. Sharma, S.; Krishna, K.V.M.; Joshi, S.S.; Radhakrishnan, M.; Palaniappan, S.; Dussa, S.; Banerjee, R.; Dahotre, N.B. Laser based additive manufacturing of tungsten: Multi-scale thermo-kinetic and thermo-mechanical computational model and experiments. *Acta Mater.* **2023**, *259*, 119244. [CrossRef]
99. Mukherjee, T.; DebRoy, T. A digital twin for rapid qualification of 3D printed metallic components. *Appl. Mater. Today* **2019**, *14*, 59–65. [CrossRef]
100. Ledford, C.; Fernandez-Zelaia, P.; Graening, T.; Campbell, Q.; Rojas, J.O.; Rossy, A.M.; Kato, Y.; Kirka, M.M. Microstructure and high temperature properties of tungsten processed via electron beam melting additive manufacturing. *Int. J. Refract. Met. Hard Mater.* **2023**, *113*, 106148. [CrossRef]
101. Matthews, M.; Trapp, J.; Guss, G.; Rubenchik, A. Direct measurements of laser absorptivity during metal melt pool formation associated with powder bed fusion additive manufacturing processes. *J. Laser Appl.* **2018**, *30*, 032302. [CrossRef]
102. Enneti, R.; Morgan, R.; Wolfe, T.; Harooni, A.; Volk, S. Direct Metal Laser Sintering (DMLS) of Tungsten Powders. In Proceedings of the Additive Manufacturing with Powder Metallurgy, Las Vegas, NV, USA, 13–15 June 2017.
103. Li, J.; Wei, Z.; Zhou, B.; Wu, Y.; Chen, S.-G.; Sun, Z. Densification, Microstructure and Properties of 90W-7Ni-3Fe Fabricated by Selective Laser Melting. *Metals* **2019**, *9*, 884. [CrossRef]
104. Hu, Z.; Liu, Y.; Chen, S.; Liu, S.; Yu, L.; Liu, Y.; Ma, Z. Achieving high-performance pure tungsten by additive manufacturing: Processing, microstructural evolution and mechanical properties. *Int. J. Refract. Met. Hard Mater.* **2023**, *113*, 106211. [CrossRef]
105. Müller, A.V.; Dorow-Gerspach, D.; Balden, M.; Binder, M.; Buschmann, B.; Curzadd, B.; Loewenhoff, T.; Neu, R.; Schlick, G.; You, J.H. Progress in additive manufacturing of pure tungsten for plasma-facing component applications. *J. Nucl. Mater.* **2022**, *566*, 153760. [CrossRef]
106. Xia, Y.; Dong, Z.; Guo, X.; Tian, Q.; Liu, Y. Towards a circular metal additive manufacturing through recycling of materials: A mini review. *J. Cent. South. Univ.* **2020**, *27*, 1134–1145. [CrossRef]
107. Gradl, P.; Mireles, O.R.; Andrews, N. Introduction to Additive Manufacturing for Propulsion and Energy Systems. In Proceedings of the AIAA Propulsion and Energy Forum 2021, Denver, CO, USA, 9–11 August 2021.
108. Sidambe, A.; Fox, P. Analysis of melt pool during the laser powder bed fusion of tungsten. In Proceedings of the RAPDASA 2019 Conference and Exhibition, Gqeberha, South Africa, 28–31 October 2019.
109. Sochalski-Kolbus, L.M.; Payzant, E.A.; Cornwell, P.A.; Watkins, T.R.; Babu, S.S.; Dehoff, R.R.; Lorenz, M.; Ovchinnikova, O.; Duty, C. Comparison of Residual Stresses in Inconel 718 Simple Parts Made by Electron Beam Melting and Direct Laser Metal Sintering. *Metall. Mater. Trans. A* **2015**, *46*, 1419–1432. [CrossRef]
110. Xue, J.; Feng, Z.; Tang, J.; Tang, C.; Zhao, Z. Selective laser melting additive manufacturing of tungsten with niobium alloying: Microstructure and suppression mechanism of microcracks. *J. Alloys Compd.* **2021**, *874*, 159879. [CrossRef]
111. Ng, G.K.L.; Jarfors, A.E.W.; Bi, G.; Zheng, H.Y. Porosity formation and gas bubble retention in laser metal deposition. *Appl. Phys. A* **2009**, *97*, 641–649. [CrossRef]

112. Zhong, M.; Liu, W.; Ning, G.; Yang, L.; Chen, Y. Laser direct manufacturing of tungsten nickel collimation component. *J. Mater. Process Technol.* **2004**, *147*, 167–173. [CrossRef]
113. Li, J.; Wu, Y.; Zhou, B.; Wei, Z. Laser Powder Bed Fusion of Pure Tungsten: Effects of Process Parameters on Morphology. *Densif. Microstruct. Mater.* **2020**, *14*, 165. [CrossRef]
114. Dong, J.; Liu, S.; Chen, H.; Li, D.; Zhang, T.; Chen, C.; Zhou, K. Effect of atmosphere on the microstructure and properties of additively manufactured tungsten. *Mater. Sci. Technol.* **2020**, *36*, 1988–1996. [CrossRef]
115. Huang, J.; Li, M.; Wang, J.; Pei, Z.; Mclntyre, P.; Ma, C. Selective laser melting of tungsten: Effects of hatch distance and point distance on pore formation. *J. Manuf. Process* **2021**, *61*, 296–302. [CrossRef]
116. Adamson, A.W. Potential distortion model for contact angle and spreading. II. Temperature dependent effects. *J. Colloid. Interface Sci.* **1973**, *44*, 273–281. [CrossRef]
117. Muramatsu, Y.; Halada, K.; Dan, T.; Isoda, Y. Solid-Liquid Interfacial Tension of the W-Cu System. *J. Jpn. Inst. Met.* **1990**, *54*, 679–684. [CrossRef]
118. Pan, S.; Guan, Z.; Yao, G.; Yuan, J.; Li, X. Mo-enhanced chemical stability of TiC nanoparticles in molten Al. *J. Alloys Compd.* **2021**, *856*, 158169. [CrossRef]
119. Wei, C.; Gu, H.; Gu, Y.; Liu, L.; Huang, Y.; Cheng, D.; Li, Z.; Li, L. Abnormal interfacial bonding mechanisms of multi-material additive-manufactured tungsten–stainless steel sandwich structure. *Int. J. Extrem. Manuf.* **2022**, *4*, 025002. [CrossRef]
120. Li, K.; Wang, D.; Xing, L.; Wang, Y.; Yu, C.; Chen, J.; Zhang, T.; Ma, J.; Liu, W.; Shen, Z. Crack suppression in additively manufactured tungsten by introducing secondary-phase nanoparticles into the matrix. *Int. J. Refract. Met. Hard Mater.* **2019**, *79*, 158–163. [CrossRef]
121. Kurishita, H.; Matsuo, S.; Arakawa, H.; Sakamoto, T.; Kobayashi, S.; Nakai, K.; Okano, H.; Watanabe, H.; Yoshida, N.; Torikai, Y.; et al. Current status of nanostructured tungsten-based materials development. *Phys. Scr. T* **2014**, *159*, 014032. [CrossRef]
122. Nagy, D.; Humphry-Baker, S.A. An oxidation mechanism map for tungsten. *Scr. Mater.* **2022**, *209*, 114373. [CrossRef]
123. Warren, A.; Nylund, A.; Olefjord, I. Oxidation of tungsten and tungsten carbide in dry and humid atmospheres. *Int. J. Refract. Met. Hard Mater.* **1996**, *14*, 345–353. [CrossRef]
124. Savitskii, E.M.; Burkhanov, G.S. *Physical Metallurgy of Refractory Metals and Alloys*; Springer US: Boston, MA, USA, 1995. [CrossRef]
125. Naghshineh, B.; Ribeiro, A.; Jacinto, C.; Carvalho, H. Social impacts of additive manufacturing: A stakeholder-driven framework. *Technol. Forecast. Soc. Chang.* **2021**, *164*, 120368. [CrossRef]
126. Antusch, S.; Klein, A.; Baumgärtner, S.; Bonnekoh, C.; Böswirth, B.; Dorow-Gerspach, D.; Dietrich, S.; Ehrhardt, M.; Ghidersa, B.-E.; Greuner, H.; et al. Additive manufacturing of novel complex tungsten components via electron beam melting: Basic properties and evaluation of the high heat flux behavior. *Nucl. Mater. Energy* **2024**, *39*, 101683. [CrossRef]
127. Eckley, C.C.; Kemnitz, R.A.; Fassio, C.P.; Hartsfield, C.R.; Leonhardt, T.A. Selective Laser Melting of Tungsten-Rhenium Alloys. *JOM* **2021**, *73*, 3439–3450. [CrossRef]
128. Yamamoto, T.; Hara, M.; Hatano, Y. Cracking behavior and microstructural. mechanical and thermal characteristics of tungsten–rhenium binary alloys fabricated by laser powder bed fusion. *Int. J. Refract. Metals Hard Mater.* **2021**, *100*, 105651. [CrossRef]
129. Klopp, W.; Witzke, W.; Raffo, P. Mechanical Properties of Dilute Tungsten-Rhenium Alloys. 1966. Available online: https://www.semanticscholar.org/paper/Mechanical-properties-of-dilute-tungsten-rhenium-Klopp-Witzke/f3a5af30bb932de1537aaa486f215920185ab265 (accessed on 15 July 2024).
130. Zhang, D.Q.; Liu, Z.H.; Cai, Q.Z.; Liu, J.H.; Chua, C.K. Influence of Ni content on microstructure of W–Ni alloy produced by selective laser melting. *Int. J. Refract. Met. Hard Mater.* **2014**, *45*, 15–22. [CrossRef]
131. Zhang, D.; Cai, Q.; Liu, J.; Li, R. Research on Process and Microstructure Formation of W-Ni-Fe Alloy Fabricated by Selective Laser Melting. *J. Mater. Eng. Perform.* **2011**, *20*, 1049–1054. [CrossRef]
132. Iveković, A.; Montero-Sistiaga, M.L.; Vanmeensel, K.; Kruth, J.-P.; Vleugels, J. Effect of processing parameters on microstructure and properties of tungsten heavy alloys fabricated by SLM. *Int. J. Refract. Met. Hard Mater.* **2019**, *82*, 23–30. [CrossRef]
133. Hu, Z.; Liu, Y.; Wu, J.; Dong, J.; Ma, Z.; Liu, Y. The simultaneous improvement of strength and ductility of the 93W-4.6Ni-2.4Fe prepared by additive manufacturing via optimizing sintering post-treatment. *Addit. Manuf.* **2021**, *46*, 102216. [CrossRef]
134. Chen, H.; Zi, X.; Han, Y.; Dong, J.; Liu, S.; Chen, C. Microstructure and mechanical properties of additive manufactured W-Ni-Fe-Co composite produced by selective laser melting. *Int. J. Refract. Met. Hard Mater.* **2020**, *86*, 105111. [CrossRef]
135. Wang, M.; Li, R.; Yuan, T.; Chen, C.; Zhang, M.; Weng, Q.; Yuan, J. Selective laser melting of W-Ni-Cu composite powder: Densification, microstructure evolution and nano-crystalline formation. *Int. J. Refract. Met. Hard Mater.* **2018**, *70*, 9–18. [CrossRef]
136. Yan, A.; Wang, Z.; Yang, T.; Wang, Y.; Ma, Z. Microstructure, thermal physical property and surface morphology of W-Cu composite fabricated via selective laser melting. *Mater. Des.* **2016**, *109*, 79–87. [CrossRef]
137. Li, R.; Shi, Y.; Liu, J.; Xie, Z.; Wang, Z. Selective laser melting W–10 wt.% Cu composite powders. *Int. J. Adv. Manuf. Technol.* **2010**, *48*, 597–605. [CrossRef]
138. Wang, G.; Qin, Y.; Yang, S. Characterization of laser-powder interaction and particle transport phenomena during laser direct deposition of W–Cu composite. *Addit. Manuf.* **2021**, *37*, 101722. [CrossRef]
139. Zhou, Z.; Tan, Z.; He, D.; Zhou, Z.; Cui, L.; Wang, Y.; Shao, W.; Wang, G. Fabrication of three-dimensional connected W-Cu10Sn composites by selective laser melting. *Mater. Lett.* **2020**, *264*, 127377. [CrossRef]
140. Li, K.; Li, Y.; Chen, W.; Zhao, C.; Yuan, Y.; Cheng, L.; Morgan, T.W.; Liu, W.; Shen, Z. Effect of Ta addition on the fuzz formation of additively manufactured W-based materials. *Nucl. Fusion.* **2020**, *60*, 064004. [CrossRef]

141. Li, K.; Ma, G.; Xing, L.; Wang, Y.; Yu, C.; Chen, J.; Ma, J.; Wu, G.; Liu, W.; Shen, Z.; et al. Crack suppression via in-situ oxidation in additively manufactured W-Ta alloy. *Mater. Lett.* **2020**, *263*, 127212. [CrossRef]
142. Guo, Z.; Wang, L.; Wang, X.-Z. Additive manufacturing of W-12Ta(wt%) alloy: Processing and resulting mechanical properties. *J. Alloys Compd.* **2021**, *868*, 159193. [CrossRef]
143. Li, J.; Wei, Z.; Zhou, B.; Wu, Y.; Chen, S.-G.; Sun, Z. Preparation, microstructure, and microhardness of selective laser-melted W–3Ta sample. *J. Mater. Res.* **2020**, *35*, 2016–2024. [CrossRef]
144. Xiao, B.; Jia, W.; Tang, H.; Wang, J.; Zhou, L. Microstructure and mechanical properties of a newly developed WTaRe refractory alloy by selective electron beam melting. *Addit. Manuf.* **2022**, *54*, 102738. [CrossRef]
145. Xiao, B.; Jia, W.; Wang, J.; Zhou, L. High-temperature mechanical behaviors of a WTaRe refractory alloy manufactured by selective electron beam melting. *Int. J. Refract. Met. Hard Mater.* **2023**, *116*, 106371. [CrossRef]
146. Chen, H.; Ye, L.; Han, Y.; Chen, C.; Fan, J. Additive manufacturing of W–Fe composites using laser metal deposition: Microstructure, phase transformation, and mechanical properties. *Mater. Sci. Eng. A* **2021**, *811*, 141036. [CrossRef]
147. Tan, Z.; Zhou, Z.; Wu, X.; Wang, Y.; Shao, W.; Guo, X.; Zhou, Z.; Yang, Y.; Wang, G.; He, D. In situ synthesis of spherical W Mo alloy powder for additive manufacturing by spray granulation combined with thermal plasma spheroidization. *Int. J. Refract. Met. Hard Mater.* **2021**, *95*, 105460. [CrossRef]
148. Lang, S.; Sun, N.; Cao, J.; Yu, W.; Yang, Z.; Hou, S. Fabrication of Ultra-Fine-Grained W-TiC Alloys by a Simple Ball-Milling and Hydrogen Reduction Method. *Materials* **2021**, *14*, 5865. [CrossRef] [PubMed]
149. Gu, D.; Dai, D.; Chen, W.; Chen, H. Selective Laser Melting Additive Manufacturing of Hard-to-Process Tungsten-Based Alloy Parts with Novel Crystalline Growth Morphology and Enhanced Performance. *J. Manuf. Sci. Eng.* **2016**, *138*, 081003. [CrossRef]
150. Chen, J.; Zhao, C.; Li, K.; Li, M.; Sun, S.; Zhang, S.; Ma, J.; Liu, W. Effect of TaC addition on microstructure and microhardness of additively manufactured tungsten. *J. Alloys Compd.* **2022**, *897*, 162978. [CrossRef]
151. Cole, N.C.; Gilliland, R.G.; Slaughter, G.M. Weldability of tungsten and its alloys. In Proceedings of the American Welding Society 49th Annual Meeting, Chicago, IL, USA, 1–5 April 1968.
152. Bose, A.; German, R.M. Microstructural refinement of W-Ni-Fe heavy alloys by alloying additions. *Metall. Trans. A* **1988**, *19*, 3100–3103. [CrossRef]
153. Luo, A.; Jacobson, D.L.; Shin, K.S. Solution softening mechanism of iridium and rhenium in tungsten at room temperature. *Int. J. Refract. Met. Hard Mater.* **1991**, *10*, 107–114. [CrossRef]
154. Wang, Y.K.; Xie, Z.M.; Wang, M.M.; Deng, H.W.; Yang, J.F.; Jiang, Y.; Zhang, T.; Wang, X.P.; Fang, Q.F.; Liu, C.S. The superior thermal stability and tensile properties of hot rolled W-HfC alloys. *Int. J. Refract. Met. Hard Mater.* **2019**, *81*, 42–48. [CrossRef]
155. Leonhardt, T. Properties of tungsten-rhenium and tungsten-rhenium with hafnium carbide. *JOM* **2009**, *61*, 68–71. [CrossRef]
156. Ren, C.; Fang, Z.Z.; Koopman, M.; Butler, B.; Paramore, J.; Middlemas, S. Methods for improving ductility of tungsten—A review. *Int. J. Refract. Met. Hard Mater.* **2018**, *75*, 170–183. [CrossRef]
157. Calvo, A.; Schlueter, K.; Tejado, E.; Pintsuk, G.; Ordás, N.; Iturriza, I.; Neu, R.; Pastor, J.Y.; García-Rosales, C. Self-passivating tungsten alloys of the system W-Cr-Y for high temperature applications. *Int. J. Refract. Met. Hard Mater.* **2018**, *73*, 29–37. [CrossRef]
158. Zhang, Y.; Huang, Y.; Liu, W.; Ma, Y.; Wang, Y.; Liang, C. Effect of tantalum addition method on microstructure and mechanical properties of the 90(W 20Ta)–Ni–Fe alloy. *Int. J. Refract. Met. Hard Mater.* **2022**, *105*, 105848. [CrossRef]
159. Chen, B.; Li, Z.-B.; Liu, J.-R.; Zhang, G.-H. Effect of molybdenum addition on microstructure and mechanical properties of 90% tungsten heavy alloys. *Int. J. Refract. Met. Hard Mater.* **2022**, *106*, 105868. [CrossRef]
160. Xie, Z.M.; Liu, R.; Miao, S.; Yang, X.D.; Zhang, T.; Wang, X.P.; Fang, Q.F.; Liu, C.S.; Luo, G.N.; Lian, Y.Y.; et al. Extraordinary high ductility/strength of the interface designed bulk W-ZrC alloy plate at relatively low temperature. *Sci. Rep.* **2015**, *5*, 16014. [CrossRef] [PubMed]
161. Suman, V.; Chaira, D. Improvement of Oxidation Resistance in Tungsten Heavy Alloys through Si, Y2O3, Ni, and Co Addition. *J. Mater. Eng. Perform.* **2023**, *33*, 5279–5290. [CrossRef]
162. Yin, C.; Terentyev, D.; Zhang, T.; Nogami, S.; Antusch, S.; Chang, C.-C.; Petrov, R.H.; Pardoen, T. Ductile to brittle transition temperature of advanced tungsten alloys for nuclear fusion applications deduced by miniaturized three-point bending tests. *Int. J. Refract. Met. Hard Mater.* **2021**, *95*, 105464. [CrossRef]
163. Sharma, S.; Joshi, S.S.; Pantawane, M.V.; Radhakrishnan, M.; Mazumder, S.; Dahotre, N.B. Multiphysics multi-scale computational framework for linking process–structure–property relationships in metal additive manufacturing: A critical review. *Int. Mater. Rev.* **2023**, *68*, 943–1009. [CrossRef]